
27. PASSAGE OF PARTICLES THROUGH MATTER	2
27.1. Notation	2
27.2. Electronic energy loss by heavy particles	3
27.2.1. Moments and cross sections	3
27.2.2. Stopping power at intermediate energies	4
27.2.3. Energy loss at low energies	8
27.2.4. Density effect	10
27.2.5. Energetic knock-on electrons (δ rays)	11
27.2.6. Restricted energy loss rates for relativistic ionizing particles	11
27.2.7. Fluctuations in energy loss	12
27.2.8. Energy loss in mixtures and compounds	13
27.2.9. Ionization yields	14
27.3. Multiple scattering through small angles	15
27.4. Photon and electron interactions in matter	17
27.4.1. Radiation length	17
27.4.2. Energy loss by electrons	18
27.4.3. Critical energy	22
27.4.4. Energy loss by photons	24
27.4.5. Bremsstrahlung and pair production at very high energies	26
27.4.6. Photonuclear and electronuclear interactions at still higher energies	27
27.5. Electromagnetic cascades	27
27.6. Muon energy loss at high energy	30
27.7. Cherenkov and transition radiation	32

27. PASSAGE OF PARTICLES THROUGH MATTER

Revised January 2010 by H. Bichsel (University of Washington), D.E. Groom (LBNL), and S.R. Klein (LBNL).

27.1. Notation

Table 27.1: Summary of variables used in this section. The kinematic variables β and γ have their usual meanings.

Symbol	Definition	Units or Value
α	Fine structure constant ($e^2/4\pi\epsilon_0\hbar c$)	1/137.035 999 11(46)
M	Incident particle mass	MeV/ c^2
E	Incident part. energy $\gamma M c^2$	MeV
T	Kinetic energy	MeV
$m_e c^2$	Electron mass $\times c^2$	0.510 998 918(44) MeV
r_e	Classical electron radius $e^2/4\pi\epsilon_0 m_e c^2$	2.817 940 325(28) fm
N_A	Avogadro's number	$6.022\,1415(10) \times 10^{23} \text{ mol}^{-1}$
ze	Charge of incident particle	
Z	Atomic number of absorber	
A	Atomic mass of absorber	g mol $^{-1}$
K/A	$4\pi N_A r_e^2 m_e c^2 / A$	0.307 075 MeV g $^{-1}$ cm 2 for $A = 1 \text{ g mol}^{-1}$
I	Mean excitation energy	eV (<i>Nota bene!</i>)
$\delta(\beta\gamma)$	Density effect correction to ionization energy loss	
$\hbar\omega_p$	Plasma energy ($\sqrt{4\pi N_e r_e^3} m_e c^2 / \alpha$)	$\sqrt{\rho \langle Z/A \rangle} \times 28.816 \text{ eV}$ (ρ in g cm $^{-2}$)
N_c	Electron density	(units of r_e) $^{-3}$
w_j	Weight fraction of the j th element in a compound or mixture	
n_j	\propto number of j th kind of atoms in a compound or mixture	
—	$4\alpha r_e^2 N_A / A$	(716.408 g cm $^{-2}$) $^{-1}$ for $A = 1 \text{ g mol}^{-1}$
X_0	Radiation length	g cm $^{-2}$
E_c	Critical energy for electrons	MeV
$E_{\mu c}$	Critical energy for muons	GeV
E_s	Scale energy $\sqrt{4\pi/\alpha} m_e c^2$	21.2052 MeV
R_M	Molière radius	g cm $^{-2}$

27.2. Electronic energy loss by heavy particles [1–32]

27.2.1. Moments and cross sections :

The electronic interactions of fast charged particles with speed $v = \beta c$ occur in *single collisions with energy losses* E [1], leading to ionization, atomic, or collective excitation. Most frequently the energy losses are small (for 90% of all collisions the energy losses are less than 100 eV). In thin absorbers few collisions will take place and the total energy loss will show a large variance [1]; also see Sec. 27.2.7 below. For particles with charge ze more massive than electrons (“heavy” particles), scattering from free electrons is adequately described by the Rutherford differential cross section [2], *

$$\frac{d\sigma_R(E; \beta)}{dE} = \frac{2\pi r_e^2 m_e c^2 z^2}{\beta^2} \frac{(1 - \beta^2 E/T_{\max})}{E^2}, \quad (27.1)$$

where T_{\max} is the maximum energy transfer possible in a single collision. But in matter electrons are not free. E must be finite and depends on atomic and bulk structure. For electrons bound in atoms Bethe [3] used “Born Theorie” to obtain the differential cross section

$$\frac{d\sigma_B(E; \beta)}{dE} = \frac{d\sigma_R(E, \beta)}{dE} B(E). \quad (27.2)$$

Examples of $B(E)$ and $d\sigma_B/dE$ can be seen in Figs. 5 and 6 of Ref. 1.

Bethe’s theory extends only to some energy above which atomic effects were not important. The free-electron cross section (Eq. (27.1)) can be used to extend the cross section to T_{\max} . At high energies σ_B is further modified by polarization of the medium, and this “density effect,” discussed in Sec. 27.2.4, must also be included. Less important corrections are also discussed below.

The mean number of collisions with energy loss between E and $E + dE$ occurring in a distance δx is $N_e \delta x (d\sigma/dE) dE$, where $\sigma(E; \beta)/dx$ contains all contributions. It is convenient to define the moments

$$M_j(\beta) = N_e \delta x \int E^j \frac{d\sigma(E; \beta)}{dE} dE,$$

so that M_0 is the mean number of collisions in δx , M_1 is the mean energy loss in δx , $M_2 - M_1^2$ is the variance, *etc.* The number of collisions is Poisson-distributed with mean M_0 . N_e is either measured in electrons/(g cm^{−2}) ($N_e = N_A Z/A$) or electrons/cm³ ($N_e = N_A \rho Z/A$). The former is used throughout this chapter, since quantities of interest (dE/dx , X_0 , *etc.*) vary smoothly with composition when there is no density dependence.

* For spin 0 particles. The β dependence in the parentheses is different for spin 1/2 and spin 1 particles, but it is not important except at energies far above atomic binding energies.

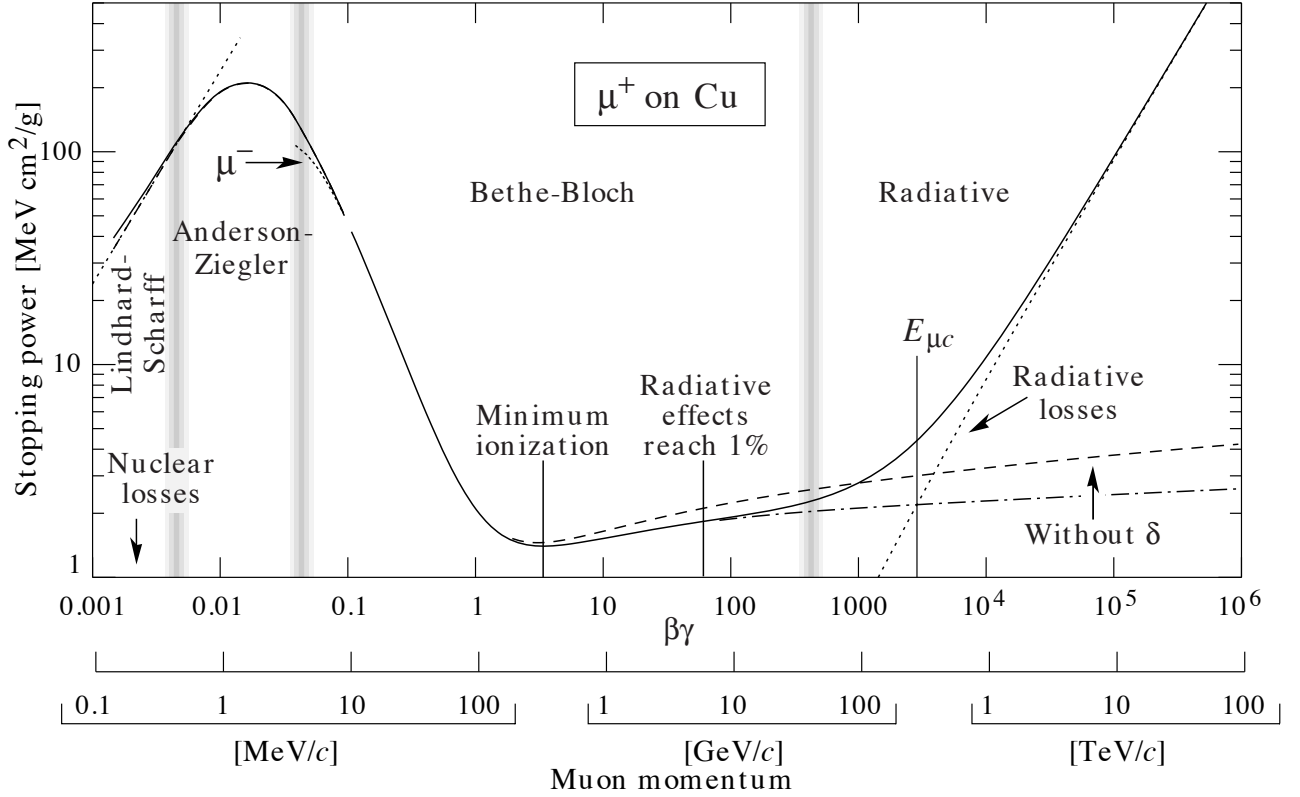


Fig. 27.1: Stopping power ($= \langle -dE/dx \rangle$) for positive muons in copper as a function of $\beta\gamma = p/Mc$ over nine orders of magnitude in momentum (12 orders of magnitude in kinetic energy). Solid curves indicate the total stopping power. Data below the break at $\beta\gamma \approx 0.1$ are taken from ICRU 49 [4], and data at higher energies are from Ref. 5. Vertical bands indicate boundaries between different approximations discussed in the text. The short dotted lines labeled “ μ^- ” illustrate the “Barkas effect,” the dependence of stopping power on projectile charge at very low energies [6].

27.2.2. Stopping power at intermediate energies :

The mean rate of energy loss by moderately relativistic charged heavy particles, $M_1/\delta x$, is well-described by the “Bethe-Bloch” equation,

$$-\left\langle \frac{dE}{dx} \right\rangle = K z^2 \frac{Z}{A} \frac{1}{\beta^2} \left[\frac{1}{2} \ln \frac{2m_e c^2 \beta^2 \gamma^2 T_{\max}}{I^2} - \beta^2 - \frac{\delta(\beta\gamma)}{2} \right]. \quad (27.3)$$

It describes the mean rate of energy loss in the region $0.1 \lesssim \beta\gamma \lesssim 1000$ for intermediate- Z materials with an accuracy of a few %. At the lower limit the projectile velocity becomes comparable to atomic electron “velocities” (Sec. 27.2.3),

and at the upper limit radiative effects begin to be important (Sec. 27.6). Both limits are Z dependent. Here T_{\max} is the maximum kinetic energy which can be imparted to a free electron in a single collision, and the other variables are defined in Table 27.1. A minor dependence on M at the highest energies is introduced through T_{\max} , but for all practical purposes $\langle dE/dx \rangle$ in a given material is a function of β alone. With the symbol definitions and values given in Table 27.1, the units are $\text{MeV g}^{-1}\text{cm}^2$.

Few concepts in high-energy physics are as misused as $\langle dE/dx \rangle$. The main problem is that the mean is weighted by very rare events with large single-collision energy deposits. Even with samples of hundreds of events a dependable value for the mean energy loss cannot be obtained. Far better and more easily measured is the most probable energy loss, discussed in Sec. 27.2.7. The most probable energy loss in a detector is considerably below the mean given by the Bethe-Bloch equation.

In a TPC (Sec. 28.6.4), the mean of 50%–70% of the samples with the smallest signals is often used as an estimator.

Although it must be used with cautions and caveats, $\langle dE/dx \rangle$ as described in Eq. (27.3) still forms the basis of much of our understanding of energy loss by charged particles. Extensive tables are available[5,4, pdg.lbl.gov/AtomicNuclearProperties/].

The function as computed for muons on copper is shown as the “Bethe-Bloch” region of Fig. 27.1. Mean energy loss behavior below this region is discussed in Sec. 27.2.3, and the radiative effects at high energy are discussed in Sec. 27.6. Only in the Bethe-Bloch region is it a function of β alone; the mass dependence is more complicated elsewhere. The stopping power in several other materials is shown in Fig. 27.2. Except in hydrogen, particles with the same velocity have similar rates of energy loss in different materials, although there is a slow decrease in the rate of energy loss with increasing Z . The qualitative behavior difference at high energies between a gas (He in the figure) and the other materials shown in the figure is due to the density-effect correction, $\delta(\beta\gamma)$, discussed in Sec. 27.2.4. The stopping power functions are characterized by broad minima whose position drops from $\beta\gamma = 3.5$ to 3.0 as Z goes from 7 to 100. The values of minimum ionization as a function of atomic number are shown in Fig. 27.3. In practical cases, most relativistic particles (*e.g.*, cosmic-ray muons) have mean energy loss rates close to the minimum; they are “minimum-ionizing particles,” or mip’s.

Eq. (27.3) may be integrated to find the total (or partial) “continuous slowing-down approximation” (CSDA) range R for a particle which loses energy only through ionization and atomic excitation. Since dE/dx depends only on β , R/M is a function of E/M or pc/M . In practice, range is a useful concept only for low-energy hadrons ($R \lesssim \lambda_I$, where λ_I is the nuclear interaction length), and for muons below a few hundred GeV (above which radiative effects dominate). R/M

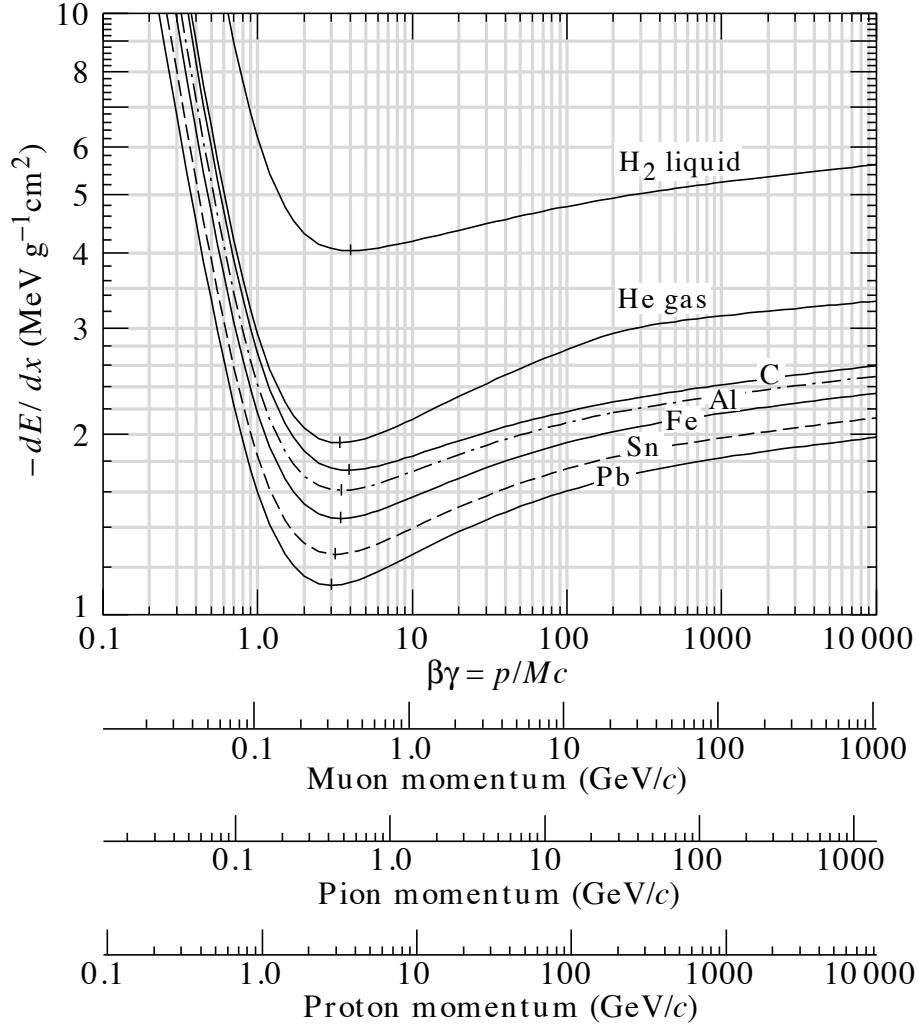


Figure 27.2: Mean energy loss rate in liquid (bubble chamber) hydrogen, gaseous helium, carbon, aluminum, iron, tin, and lead. Radiative effects, relevant for muons and pions, are not included. These become significant for muons in iron for $\beta\gamma \gtrsim 1000$, and at lower momenta for muons in higher- Z absorbers. See Fig. 27.21.

as a function of $\beta\gamma = p/Mc$ is shown for a variety of materials in Fig. 27.4.

The mass scaling of dE/dx and range is valid for the electronic losses described by the Bethe-Bloch equation, but not for radiative losses, relevant only for muons and pions.

For a particle with mass M and momentum $M\beta\gamma c$, T_{\max} is given by

$$T_{\max} = \frac{2m_e c^2 \beta^2 \gamma^2}{1 + 2\gamma m_e/M + (m_e/M)^2} . \quad (27.4)$$

In older references [2,7] the “low-energy” approximation

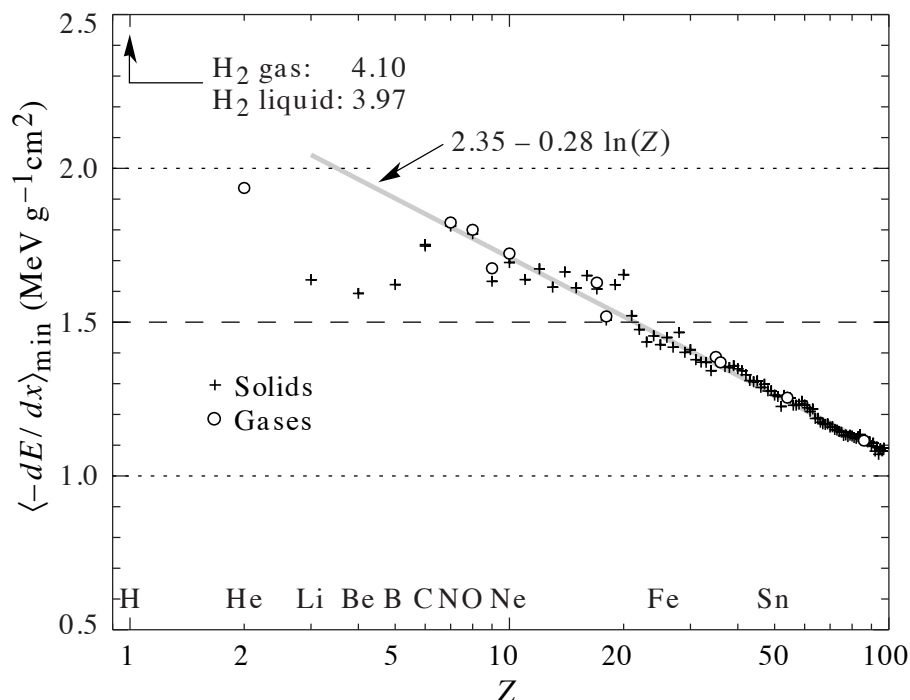


Figure 27.3: Stopping power at minimum ionization for the chemical elements. The straight line is fitted for $Z > 6$. A simple functional dependence on Z is not to be expected, since $\langle -dE/dx \rangle$ also depends on other variables.

$T_{\max} = 2m_e c^2 \beta^2 \gamma^2$, valid for $2\gamma m_e/M \ll 1$, is often implicit. For a pion in copper, the error thus introduced into dE/dx is greater than 6% at 100 GeV.

At energies of order 100 GeV, the maximum 4-momentum transfer to the electron can exceed 1 GeV/ c , where hadronic structure effects significantly modify the cross sections. This problem has been investigated by J.D. Jackson [8], who concluded that for hadrons (but not for large nuclei) corrections to dE/dx are negligible below energies where radiative effects dominate. While the cross section for rare hard collisions is modified, the average stopping power, dominated by many softer collisions, is almost unchanged.

“The determination of the mean excitation energy is the principal non-trivial task in the evaluation of the Bethe stopping-power formula” [9]. Recommended values have varied substantially with time. Estimates based on experimental stopping-power measurements for protons, deuterons, and alpha particles and on oscillator-strength distributions and dielectric-response functions were given in ICRU 49 [4]. See also ICRU 37 [10]. These values, shown in Fig. 27.5, have since been widely used. Machine-readable versions can also be found [11]. These values are widely used.

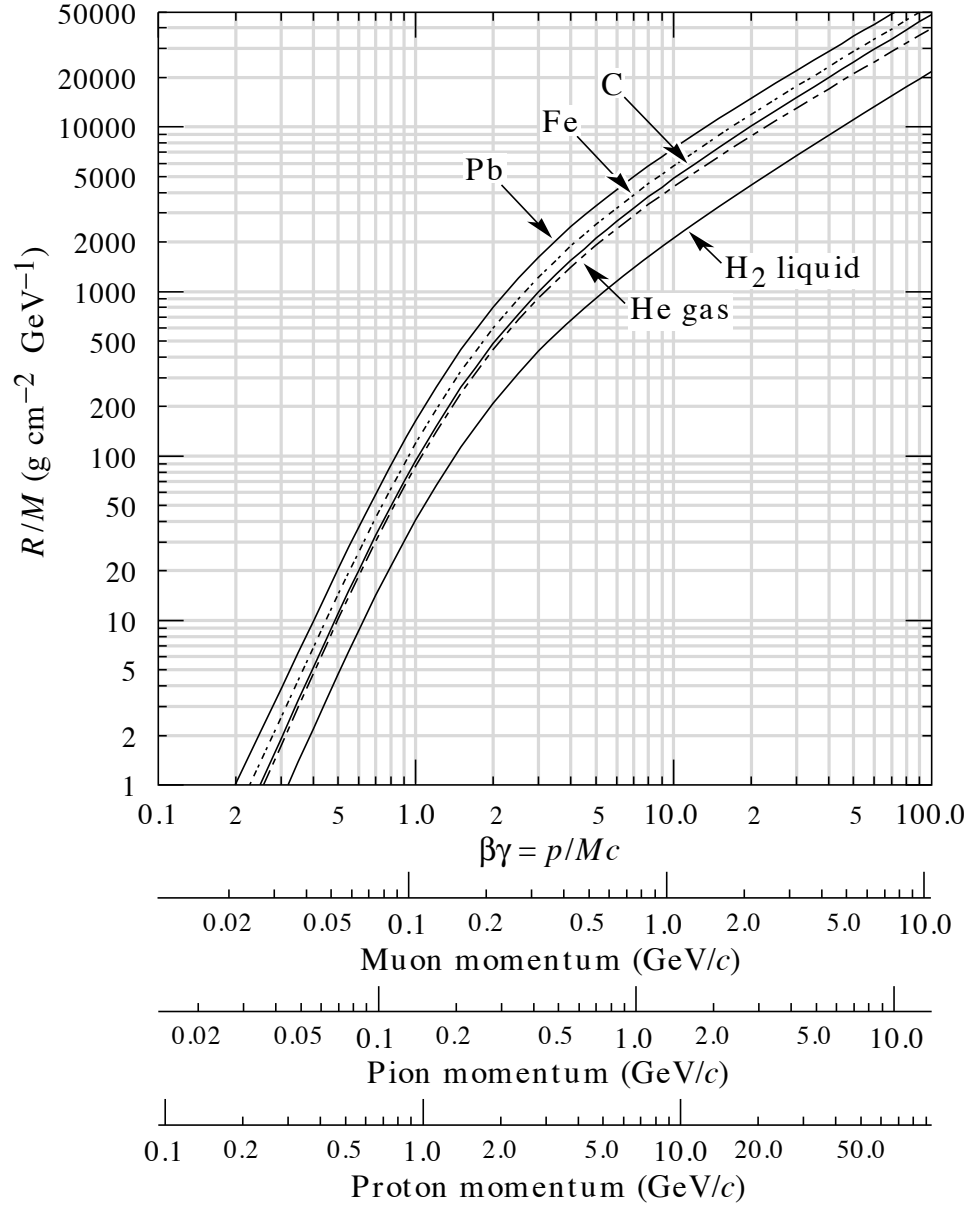


Figure 27.4: Range of heavy charged particles in liquid (bubble chamber) hydrogen, helium gas, carbon, iron, and lead. For example: For a K^+ whose momentum is 700 MeV/c, $\beta\gamma = 1.42$. For lead we read $R/M \approx 396$, and so the range is 195 g cm^{-2} .

27.2.3. Energy loss at low energies : Shell corrections C/Z must be included in the square brackets of Eq. (27.3) [4,10,12,13] to correct for atomic binding having been neglected in calculating some of the contributions to Eq. (27.3). The Barkas form [13] was used in generating Fig. 27.1. For copper it contributes about 1% at $\beta\gamma = 0.3$ (kinetic energy 6 MeV for a pion), and the correction decreases very rapidly with increasing energy.

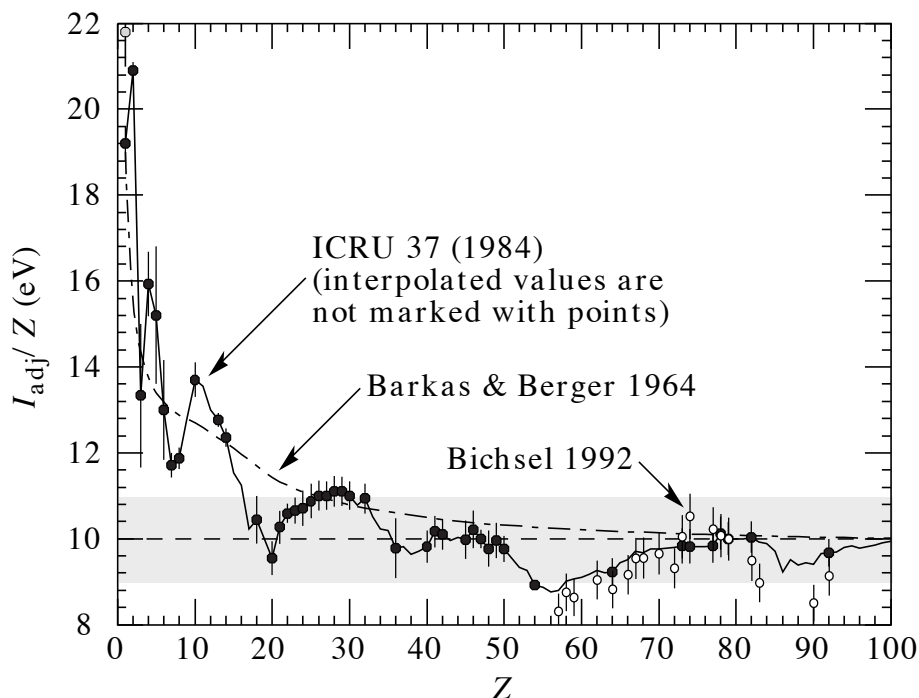


Figure 27.5: Mean excitation energies (divided by Z) as adopted by the ICRU [10]. Those based on experimental measurements are shown by symbols with error flags; the interpolated values are simply joined. The grey point is for liquid H₂; the black point at 19.2 eV is for H₂ gas. The open circles show more recent determinations by Bichsel [12]. The dotted curve is from the approximate formula of Barkas [13] used in early editions of this *Review*.

Equation 27.2, and therefore Eq. (27.3), are based on a first-order Born approximation. Higher-order corrections, again important only at lower energy, are normally included by adding the “Bloch correction” $z^2 L_2(\beta)$ inside the square brackets (Eq.(2.5) in [4]).

An additional “Barkas correction” $z L_1(\beta)$ makes the stopping power for a negative particle somewhat smaller than for a positive particle with the same mass and velocity. In a 1956 paper, Barkas *et al.* noted that negative pions had a longer range than positive pions [6]. The effect has been measured for a number of negative/positive particle pairs, most recently for antiprotons at the CERN LEAR facility [14].

A detailed discussion of low-energy corrections to the Bethe formula is given in ICRU Report 49 [4]. When the corrections are properly included, the Bethe-Bloch treatment is accurate to about 1% down to $\beta \approx 0.05$, or about 1 MeV for protons.

For $0.01 < \beta < 0.05$, there is no satisfactory theory. For protons, one usually relies on the phenomenological fitting formulae developed by Andersen and

10 27. Passage of particles through matter

Ziegler [4,15]. For particles moving more slowly than $\approx 0.01c$ (more or less the velocity of the outer atomic electrons), Lindhard has been quite successful in describing electronic stopping power, which is proportional to β [16]. Finally, we note that at even lower energies, *e.g.*, for protons of less than several hundred eV, non-ionizing nuclear recoil energy loss dominates the total energy loss [4,16,17].

As shown in ICRU 49 [4] (using data taken from Ref. 15), the nuclear plus electronic proton stopping power in copper is $113 \text{ MeV cm}^2 \text{ g}^{-1}$ at $T = 10 \text{ keV}$, rises to a maximum of $210 \text{ MeV cm}^2 \text{ g}^{-1}$ at 100–150 keV, then falls to $120 \text{ MeV cm}^2 \text{ g}^{-1}$ at 1 MeV. Above 0.5–1.0 MeV the corrected Bethe-Bloch theory is adequate.

27.2.4. Density effect : As the particle energy increases, its electric field flattens and extends, so that the distant-collision contribution to Eq. (27.3) increases as $\ln \beta\gamma$. However, real media become polarized, limiting the field extension and effectively truncating this part of the logarithmic rise [2–7,18–20]. At very high energies,

$$\delta/2 \rightarrow \ln(\hbar\omega_p/I) + \ln \beta\gamma - 1/2, \quad (27.5)$$

where $\delta(\beta\gamma)/2$ is the density effect correction introduced in Eq. (27.3) and $\hbar\omega_p$ is the plasma energy defined in Table 27.1. A comparison with Eq. (27.3) shows that $|dE/dx|$ then grows as $\ln \beta\gamma$ rather than $\ln \beta^2\gamma^2$, and that the mean excitation energy I is replaced by the plasma energy $\hbar\omega_p$. The ionization stopping power as calculated with and without the density effect correction is shown in Fig. 27.1. Since the plasma frequency scales as the square root of the electron density, the correction is much larger for a liquid or solid than for a gas, as is illustrated by the examples in Fig. 27.2.

The density effect correction is usually computed using Sternheimer's parameterization [18]:

$$\delta(\beta\gamma) = \begin{cases} 2(\ln 10)x - \overline{C} & \text{if } x \geq x_1; \\ 2(\ln 10)x - \overline{C} + a(x_1 - x)^k & \text{if } x_0 \leq x < x_1; \\ 0 & \text{if } x < x_0 \text{ (nonconductors);} \\ \delta_0 10^{2(x-x_0)} & \text{if } x < x_0 \text{ (conductors)} \end{cases} \quad (27.6)$$

Here $x = \log_{10} \eta = \log_{10}(p/Mc)$. \overline{C} (the negative of the C used in Ref. 18) is obtained by equating the high-energy case of Eq. (27.6) with the limit given in Eq. (27.5). The other parameters are adjusted to give a best fit to the results of detailed calculations for momenta below $Mc \exp(x_1)$. Parameters for elements and nearly 200 compounds and mixtures of interest are published in a variety of places, notably in Ref. 20. A recipe for finding the coefficients for nontabulated materials is given by Sternheimer and Peierls [21], and is summarized in Ref. 5.

The remaining relativistic rise comes from the $\beta^2\gamma^2$ growth of T_{max} , which in turn is due to (rare) large energy transfers to a few electrons. When these events are excluded, the energy deposit in an absorbing layer approaches a constant value, the Fermi plateau (see Sec. 27.2.6 below). At extreme energies (*e.g.*, $> 332 \text{ GeV}$

for muons in iron, and at a considerably higher energy for protons in iron), radiative effects are more important than ionization losses. These are especially relevant for high-energy muons, as discussed in Sec. 27.6.

27.2.5. Energetic knock-on electrons (δ rays) : The distribution of secondary electrons with kinetic energies $T \gg I$ is [2]

$$\frac{d^2N}{dTdx} = \frac{1}{2} K z^2 \frac{Z}{A} \frac{1}{\beta^2} \frac{F(T)}{T^2} \quad (27.7)$$

for $I \ll T \leq T_{\max}$, where T_{\max} is given by Eq. (27.4). Here β is the velocity of the primary particle. The factor F is spin-dependent, but is about unity for $T \ll T_{\max}$. For spin-0 particles $F(T) = (1 - \beta^2 T/T_{\max})$; forms for spins 1/2 and 1 are also given by Rossi [2]. For incident electrons, the indistinguishability of projectile and target means that the range of T extends only to half the kinetic energy of the incident particle. Additional formulae are given in Ref. 22. Equation (27.7) is inaccurate for T close to I .

δ rays of even modest energy are rare. For $\beta \approx 1$ particle, for example, on average only one collision with $T_e > 1$ keV will occur along a path length of 90 cm of Ar gas [1].

A δ ray with kinetic energy T_e and corresponding momentum p_e is produced at an angle θ given by

$$\cos \theta = (T_e/p_e)(p_{\max}/T_{\max}) , \quad (27.8)$$

where p_{\max} is the momentum of an electron with the maximum possible energy transfer T_{\max} .

27.2.6. Restricted energy loss rates for relativistic ionizing particles

: Further insight can be obtained by examining the mean energy deposit by an ionizing particle when energy transfers are restricted to $T \leq T_{\text{cut}} \leq T_{\max}$. The restricted energy loss rate is

$$\begin{aligned} -\frac{dE}{dx} \Big|_{T < T_{\text{cut}}} &= K z^2 \frac{Z}{A} \frac{1}{\beta^2} \left[\frac{1}{2} \ln \frac{2m_e c^2 \beta^2 \gamma^2 T_{\text{cut}}}{I^2} \right. \\ &\quad \left. - \frac{\beta^2}{2} \left(1 + \frac{T_{\text{cut}}}{T_{\max}} \right) - \frac{\delta}{2} \right] . \end{aligned} \quad (27.9)$$

This form approaches the normal Bethe-Bloch function (Eq. (27.3)) as $T_{\text{cut}} \rightarrow T_{\max}$. It can be verified that the difference between Eq. (27.3) and Eq. (27.9) is equal to $\int_{T_{\text{cut}}}^{T_{\max}} T(d^2N/dTdx)dT$, where $d^2N/dTdx$ is given by Eq. (27.7).

Since T_{cut} replaces T_{\max} in the argument of the logarithmic term of Eq. (27.3), the $\beta\gamma$ term producing the relativistic rise in the close-collision part of dE/dx is replaced by a constant, and $|dE/dx|_{T < T_{\text{cut}}}$ approaches the constant “Fermi plateau.” (The density effect correction δ eliminates the explicit $\beta\gamma$ dependence

12 27. Passage of particles through matter

produced by the distant-collision contribution.) This behavior is illustrated in Fig. 27.6, where restricted loss rates for two examples of T_{cut} are shown in comparison with the full Bethe-Bloch dE/dx and the Landau-Vavilov most probable energy loss (to be discussed in Sec. 27.2.7 below).

27.2.7. Fluctuations in energy loss : For detectors of moderate thickness x (*e.g.* scintillators or LAr cells),* the energy loss probability distribution $f(\Delta; \beta\gamma, x)$ is adequately described by the highly-skewed Landau (or Landau-Vavilov) distribution [24,25]. The most probable energy loss is [26]

$$\Delta_p = \xi \left[\ln \frac{2mc^2\beta^2\gamma^2}{I} + \ln \frac{\xi}{I} + j - \beta^2 - \delta(\beta\gamma) \right] , \quad (27.10)$$

where $\xi = (K/2) \langle Z/A \rangle (x/\beta^2)$ MeV for a detector with a thickness x in g cm^{-2} , and $j = 0.200$ [26].[†] While dE/dx is independent of thickness, Δ_p/x scales as $a \ln x + b$. The density correction $\delta(\beta\gamma)$ was not included in Landau's or Vavilov's work, but it was later included by Bichsel [26]. The high-energy behavior of $\delta(\beta\gamma)$ (Eq. (27.5)), is such that

$$\Delta_p \xrightarrow{\beta\gamma \gtrsim 100} \xi \left[\ln \frac{2mc^2\xi}{(\hbar\omega_p)^2} + j \right] . \quad (27.11)$$

Thus the Landau-Vavilov most probable energy loss, like the restricted energy loss, reaches a Fermi plateau. The Bethe-Bloch dE/dx and Landau-Vavilov-Bichsel Δ_p/x in silicon are shown as a function of muon energy in Fig. 27.6. The case $x/\rho = 1600 \mu\text{m}$ was chosen since it has about the same stopping power as does 3 mm of plastic scintillator. Folding in experimental resolution displaces the peak of the distribution, usually toward a higher value.

The mean of the energy-loss given by the Bethe-Bloch equation, Eq. (27.3), is ill-defined experimentally and is not useful for describing energy loss by single particles. (It finds its application in dosimetry, where only bulk deposit is of relevance.) It rises as $\ln \beta\gamma$ because T_{max} increases as $\beta^2\gamma^2$. The large single-collision energy transfers that increasingly extend the long tail are rare, making the mean of an experimental distribution consisting of a few hundred events subject to large fluctuations and sensitive to cuts as well as to background. The most probable energy loss should be used.

For very thick absorbers the distribution is less skewed but never approaches a Gaussian. In the case of Si illustrated in Fig. 27.6, the most probable energy loss per unit thickness for $x \approx 35 \text{ g cm}^{-2}$ is very close to the restricted energy loss with $T_{\text{cut}} = 2 dE/dx|_{\text{min}}$.

* $G \lesssim 0.05\text{--}0.1$, where G is given by Rossi [Ref. 2, Eq. 2.7.10]. It is Vavilov's κ [25].

[†] Rossi [2], Talman [27], and others give somewhat different values for j . The most probable loss is not sensitive to its value.

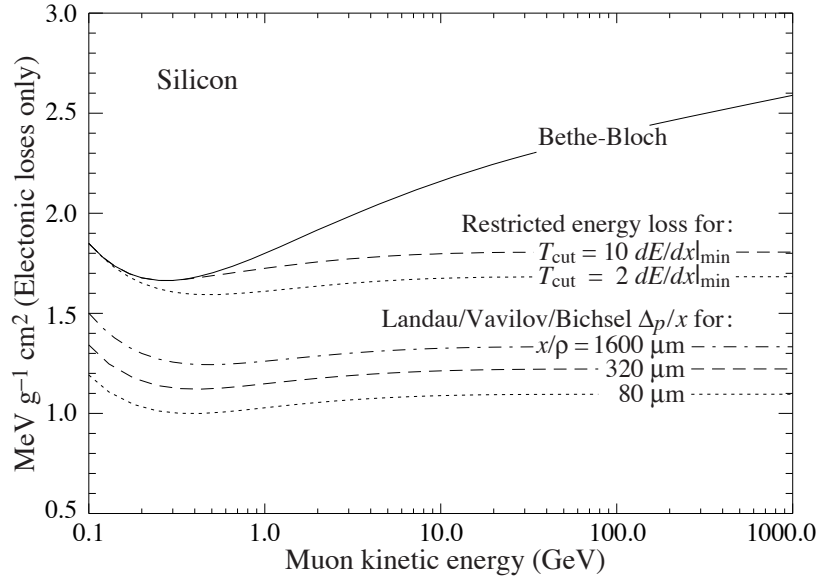


Figure 27.6: Bethe-Bloch dE/dx , two examples of restricted energy loss, and the Landau most probable energy per unit thickness in silicon. The change of Δ_p/x with thickness x illustrates its $a \ln x + b$ dependence. Minimum ionization ($dE/dx|_{\min}$) is $1.664 \text{ MeV g}^{-1} \text{ cm}^2$. Radiative losses are excluded. The incident particles are muons.

The Landau distribution fails to describe energy loss in thin absorbers such as gas TPC cells [1] and Si detectors [26], as shown clearly in Fig. 1 of Ref. 1 for an argon-filled TPC cell. Also see Talman [27]. While Δ_p/x may be calculated adequately with Eq. (27.10), the distributions are significantly wider than the Landau width $w = 4\xi$ [Ref. 26, Fig. 15]. Examples for thin silicon detectors are shown in Fig. 27.7.

27.2.8. Energy loss in mixtures and compounds : A mixture or compound can be thought of as made up of thin layers of pure elements in the right proportion (Bragg additivity). In this case,

$$\frac{dE}{dx} = \sum w_j \left. \frac{dE}{dx} \right|_j, \quad (27.12)$$

where $dE/dx|_j$ is the mean rate of energy loss (in MeV g cm^{-2}) in the j th element. Eq. (27.3) can be inserted into Eq. (27.12) to find expressions for $\langle Z/A \rangle$, $\langle I \rangle$, and $\langle \delta \rangle$; for example, $\langle Z/A \rangle = \sum w_j Z_j/A_j = \sum n_j Z_j / \sum n_j A_j$. However, $\langle I \rangle$ as defined this way is an underestimate, because in a compound electrons are more tightly bound than in the free elements, and $\langle \delta \rangle$ as calculated this way has little relevance, because it is the electron density that matters. If possible, one uses the tables given in Refs. 20 and 28, which include effective excitation energies and interpolation coefficients for calculating the density effect correction for the chemical

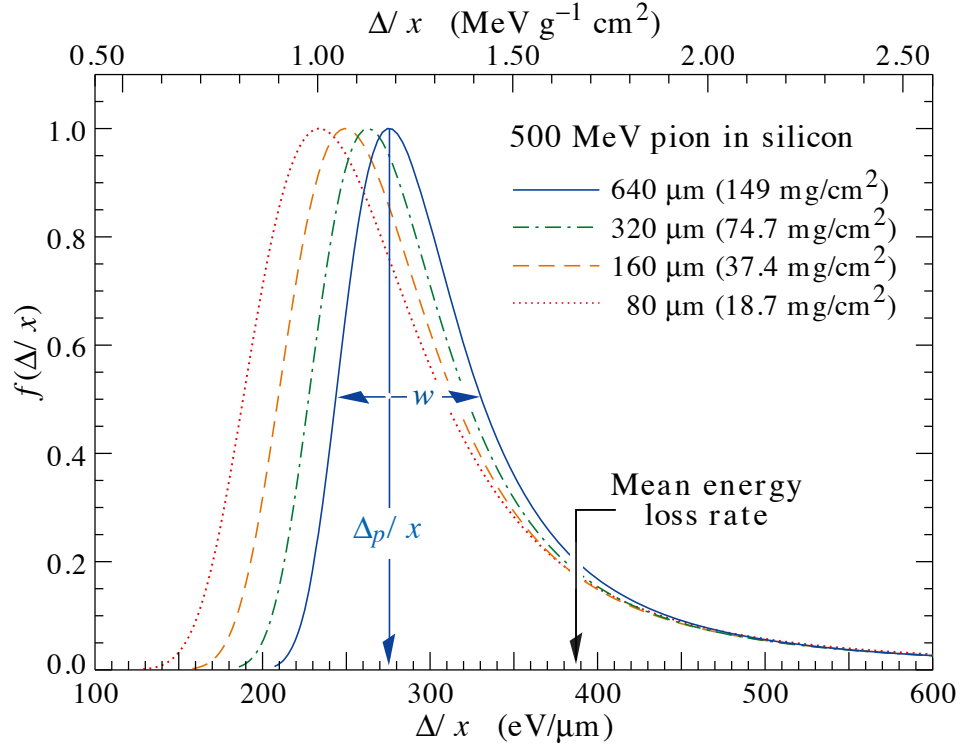


Figure 27.7: Straggling functions in silicon for 500 MeV pions, normalized to unity at the most probable value δ_p/x . The width w is the full width at half maximum.

elements and nearly 200 mixtures and compounds. If a compound or mixture is not found, then one uses the recipe for δ given in Ref. 21 (repeated in Ref. 5), and calculates $\langle I \rangle$ according to the discussion in Ref. 9. (Note the “13%” rule!)

27.2.9. Ionization yields : Physicists frequently relate total energy loss to the number of ion pairs produced near the particle’s track. This relation becomes complicated for relativistic particles due to the wandering of energetic knock-on electrons whose ranges exceed the dimensions of the fiducial volume. For a qualitative appraisal of the nonlocality of energy deposition in various media by such modestly energetic knock-on electrons, see Ref. 29. The mean local energy dissipation per local ion pair produced, W , while essentially constant for relativistic particles, increases at slow particle speeds [30]. For gases, W can be surprisingly sensitive to trace amounts of various contaminants [30]. Furthermore, ionization yields in practical cases may be greatly influenced by such factors as subsequent recombination [31].

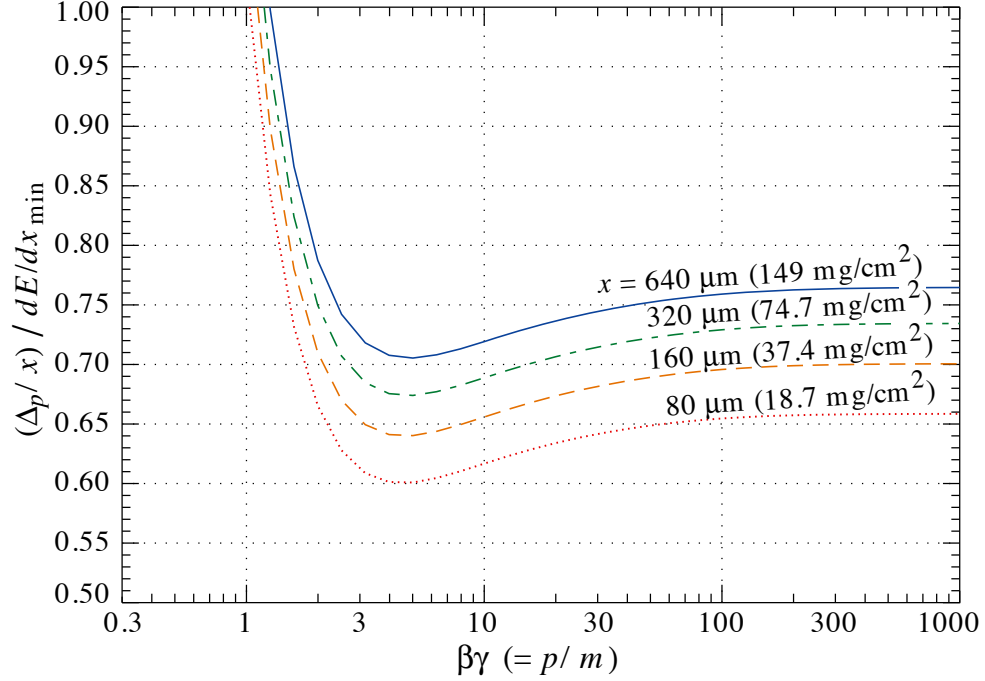


Figure 27.8: Most probable energy loss in silicon, scaled to the mean loss of a minimum ionizing particle, $388 \text{ eV}/\mu\text{m}$ ($1.66 \text{ MeV g}^{-1}\text{cm}^2$).

27.3. Multiple scattering through small angles

A charged particle traversing a medium is deflected by many small-angle scatters. Most of this deflection is due to Coulomb scattering from nuclei, and hence the effect is called multiple Coulomb scattering. (However, for hadronic projectiles, the strong interactions also contribute to multiple scattering.) The Coulomb scattering distribution is well represented by the theory of Molière [33]. It is roughly Gaussian for small deflection angles, but at larger angles (greater than a few θ_0 , defined below) it behaves like Rutherford scattering, with larger tails than does a Gaussian distribution.

If we define

$$\theta_0 = \theta_{\text{plane}}^{\text{rms}} = \frac{1}{\sqrt{2}} \theta_{\text{space}}^{\text{rms}} . \quad (27.13)$$

then it is sufficient for many applications to use a Gaussian approximation for the central 98% of the projected angular distribution, with a width given by [34,35]

$$\theta_0 = \frac{13.6 \text{ MeV}}{\beta c p} z \sqrt{x/X_0} \left[1 + 0.038 \ln(x/X_0) \right] . \quad (27.14)$$

Here p , βc , and z are the momentum, velocity, and charge number of the incident particle, and x/X_0 is the thickness of the scattering medium in radiation lengths (defined below). This value of θ_0 is from a fit to Molière distribution [33] for singly charged particles with $\beta = 1$ for all Z , and is accurate to 11% or better for $10^{-3} < x/X_0 < 100$.

16 27. Passage of particles through matter

Eq. (27.14) describes scattering from a single material, while the usual problem involves the multiple scattering of a particle traversing many different layers and mixtures. Since it is from a fit to a Molière distribution, it is incorrect to add the individual θ_0 contributions in quadrature; the result is systematically too small. It is much more accurate to apply Eq. (27.14) once, after finding x and X_0 for the combined scatterer.

Lynch and Dahl have extended this phenomenological approach, fitting Gaussian distributions to a variable fraction of the Molière distribution for arbitrary scatterers [35], and achieve accuracies of 2% or better.

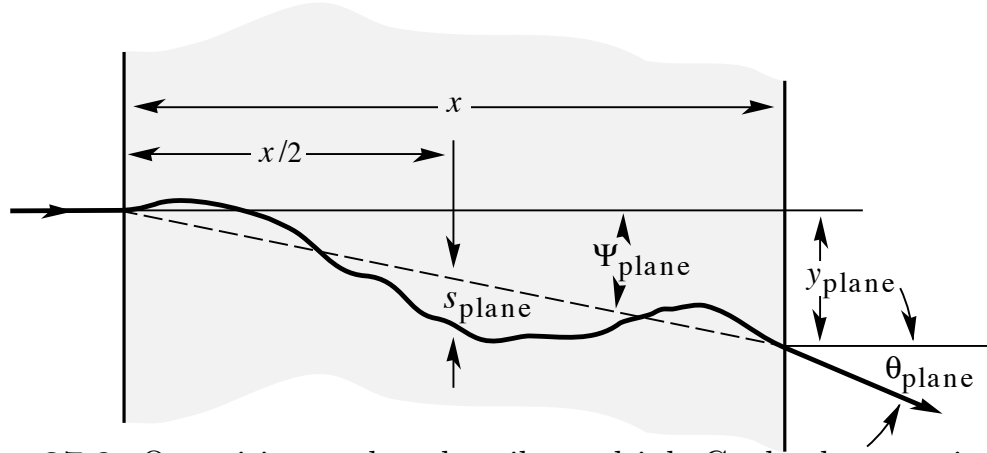


Figure 27.9: Quantities used to describe multiple Coulomb scattering. The particle is incident in the plane of the figure.

The nonprojected (space) and projected (plane) angular distributions are given approximately by [33]

$$\frac{1}{2\pi \theta_0^2} \exp \left(-\frac{\theta_{\text{space}}^2}{2\theta_0^2} \right) d\Omega , \quad (27.15)$$

$$\frac{1}{\sqrt{2\pi} \theta_0} \exp \left(-\frac{\theta_{\text{plane}}^2}{2\theta_0^2} \right) d\theta_{\text{plane}} , \quad (27.16)$$

where θ is the deflection angle. In this approximation, $\theta_{\text{space}}^2 \approx (\theta_{\text{plane},x}^2 + \theta_{\text{plane},y}^2)$, where the x and y axes are orthogonal to the direction of motion, and $d\Omega \approx d\theta_{\text{plane},x} d\theta_{\text{plane},y}$. Deflections into $\theta_{\text{plane},x}$ and $\theta_{\text{plane},y}$ are independent and identically distributed.

Figure 27.9 shows these and other quantities sometimes used to describe multiple Coulomb scattering. They are

$$\psi_{\text{plane}}^{\text{rms}} = \frac{1}{\sqrt{3}} \theta_{\text{plane}}^{\text{rms}} = \frac{1}{\sqrt{3}} \theta_0 , \quad (27.17)$$

$$y_{\text{plane}}^{\text{rms}} = \frac{1}{\sqrt{3}} x \theta_{\text{plane}}^{\text{rms}} = \frac{1}{\sqrt{3}} x \theta_0 , \quad (27.18)$$

$$s_{\text{plane}}^{\text{rms}} = \frac{1}{4\sqrt{3}} x \theta_{\text{plane}}^{\text{rms}} = \frac{1}{4\sqrt{3}} x \theta_0 . \quad (27.19)$$

All the quantitative estimates in this section apply only in the limit of small $\theta_{\text{plane}}^{\text{rms}}$ and in the absence of large-angle scatters. The random variables s , ψ , y , and θ in a given plane are distributed in a correlated fashion (see Sec. 31.1 of this *Review* for the definition of the correlation coefficient). Obviously, $y \approx x\psi$. In addition, y and θ have the correlation coefficient $\rho_{y\theta} = \sqrt{3}/2 \approx 0.87$. For Monte Carlo generation of a joint $(y_{\text{plane}}, \theta_{\text{plane}})$ distribution, or for other calculations, it may be most convenient to work with independent Gaussian random variables (z_1, z_2) with mean zero and variance one, and then set

$$\begin{aligned} y_{\text{plane}} &= z_1 x \theta_0 (1 - \rho_{y\theta}^2)^{1/2} / \sqrt{3} + z_2 \rho_{y\theta} x \theta_0 / \sqrt{3} \\ &= z_1 x \theta_0 / \sqrt{12} + z_2 x \theta_0 / 2 ; \end{aligned} \quad (27.20)$$

$$\theta_{\text{plane}} = z_2 \theta_0 . \quad (27.21)$$

Note that the second term for y_{plane} equals $x \theta_{\text{plane}}/2$ and represents the displacement that would have occurred had the deflection θ_{plane} all occurred at the single point $x/2$.

For heavy ions the multiple Coulomb scattering has been measured and compared with various theoretical distributions [36].

27.4. Photon and electron interactions in matter

27.4.1. Radiation length : High-energy electrons predominantly lose energy in matter by bremsstrahlung, and high-energy photons by e^+e^- pair production. The characteristic amount of matter traversed for these related interactions is called the radiation length X_0 , usually measured in g cm^{-2} . It is both (a) the mean distance over which a high-energy electron loses all but $1/e$ of its energy by bremsstrahlung, and (b) $\frac{7}{9}$ of the mean free path for pair production by a high-energy photon [37]. It is also the appropriate scale length for describing high-energy electromagnetic cascades. X_0 has been calculated and tabulated by Y.S. Tsai [38]:

$$\frac{1}{X_0} = 4\alpha r_e^2 \frac{N_A}{A} \left\{ Z^2 [L_{\text{rad}} - f(Z)] + Z L'_{\text{rad}} \right\} . \quad (27.22)$$

For $A = 1 \text{ g mol}^{-1}$, $4\alpha r_e^2 N_A / A = (716.408 \text{ g cm}^{-2})^{-1}$. L_{rad} and L'_{rad} are given in Table 27.2. The function $f(Z)$ is an infinite sum, but for elements up to uranium

18 27. Passage of particles through matter

can be represented to 4-place accuracy by

$$f(Z) = a^2[(1 + a^2)^{-1} + 0.20206 - 0.0369 a^2 + 0.0083 a^4 - 0.002 a^6] , \quad (27.23)$$

where $a = \alpha Z$ [39].

Table 27.2: Tsai's L_{rad} and L'_{rad} , for use in calculating the radiation length in an element using Eq. (27.22).

Element	Z	L_{rad}	L'_{rad}
H	1	5.31	6.144
He	2	4.79	5.621
Li	3	4.74	5.805
Be	4	4.71	5.924
Others	> 4	$\ln(184.15 Z^{-1/3})$	$\ln(1194 Z^{-2/3})$

Although it is easy to use Eq. (27.22) to calculate X_0 , the functional dependence on Z is somewhat hidden. Dahl provides a compact fit to the data [40]:

$$X_0 = \frac{716.4 \text{ g cm}^{-2} A}{Z(Z + 1) \ln(287/\sqrt{Z})} . \quad (27.24)$$

Results using this formula agree with Tsai's values to better than 2.5% for all elements except helium, where the result is about 5% low.

The radiation length in a mixture or compound may be approximated by

$$1/X_0 = \sum w_j/X_j , \quad (27.25)$$

where w_j and X_j are the fraction by weight and the radiation length for the j th element.

27.4.2. Energy loss by electrons : At low energies electrons and positrons primarily lose energy by ionization, although other processes (Møller scattering, Bhabha scattering, e^+ annihilation) contribute, as shown in Fig. 27.10. While ionization loss rates rise logarithmically with energy, bremsstrahlung losses rise nearly linearly (fractional loss is nearly independent of energy), and dominates above a few tens of MeV in most materials

Ionization loss by electrons and positrons differs from loss by heavy particles because of the kinematics, spin, and the identity of the incident electron with the electrons which it ionizes. Complete discussions and tables can be found in Refs. 9, 10, and 28.

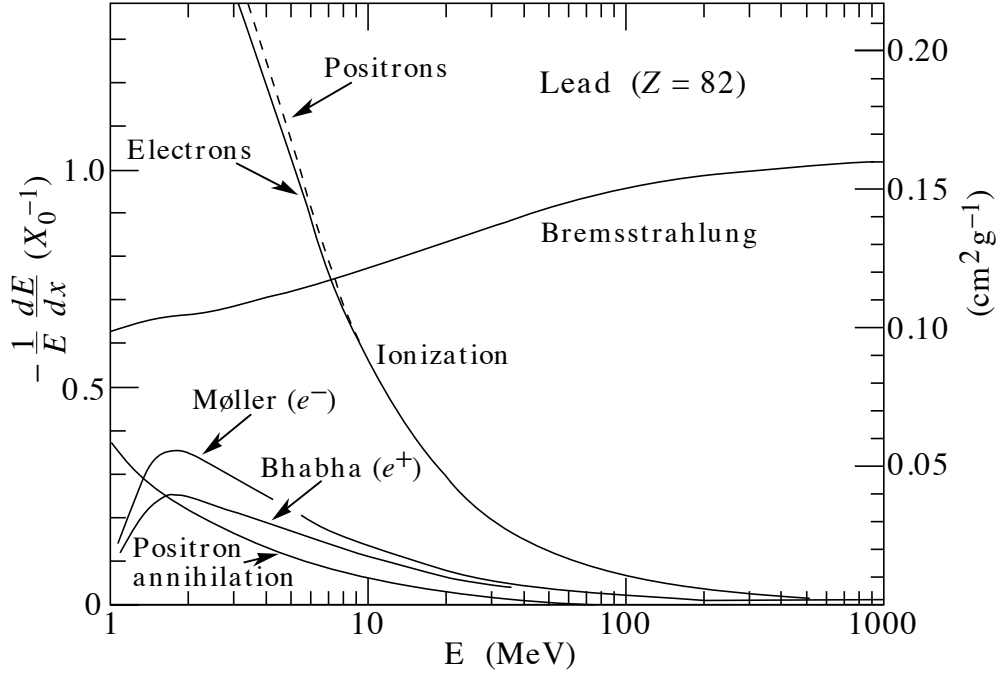


Figure 27.10: Fractional energy loss per radiation length in lead as a function of electron or positron energy. Electron (positron) scattering is considered as ionization when the energy loss per collision is below 0.255 MeV, and as Møller (Bhabha) scattering when it is above. Adapted from Fig. 3.2 from Messel and Crawford, *Electron-Photon Shower Distribution Function Tables for Lead, Copper, and Air Absorbers*, Pergamon Press, 1970. Messel and Crawford use $X_0(\text{Pb}) = 5.82 \text{ g/cm}^2$, but we have modified the figures to reflect the value given in the Table of Atomic and Nuclear Properties of Materials ($X_0(\text{Pb}) = 6.37 \text{ g/cm}^2$).

At very high energies and except at the high-energy tip of the bremsstrahlung spectrum, the cross section can be approximated in the “complete screening case” as [38]

$$d\sigma/dk = (1/k)4\alpha r_e^2 \left\{ \left(\frac{4}{3} - \frac{4}{3}y + y^2 \right) [Z^2(L_{\text{rad}} - f(Z)) + Z L'_{\text{rad}}] + \frac{1}{9}(1-y)(Z^2 + Z) \right\} , \quad (27.26)$$

where $y = k/E$ is the fraction of the electron’s energy transferred to the radiated photon. At small y (the “infrared limit”) the term on the second line ranges from 1.7% (low Z) to 2.5% (high Z) of the total. If it is ignored and the first line simplified with the definition of X_0 given in Eq. (27.22), we have

$$\frac{d\sigma}{dk} = \frac{A}{X_0 N_A k} \left(\frac{4}{3} - \frac{4}{3}y + y^2 \right) . \quad (27.27)$$

This cross section (times k) is shown by the top curve in Fig. 27.11.

This formula is accurate except in near $y = 1$, where screening may become

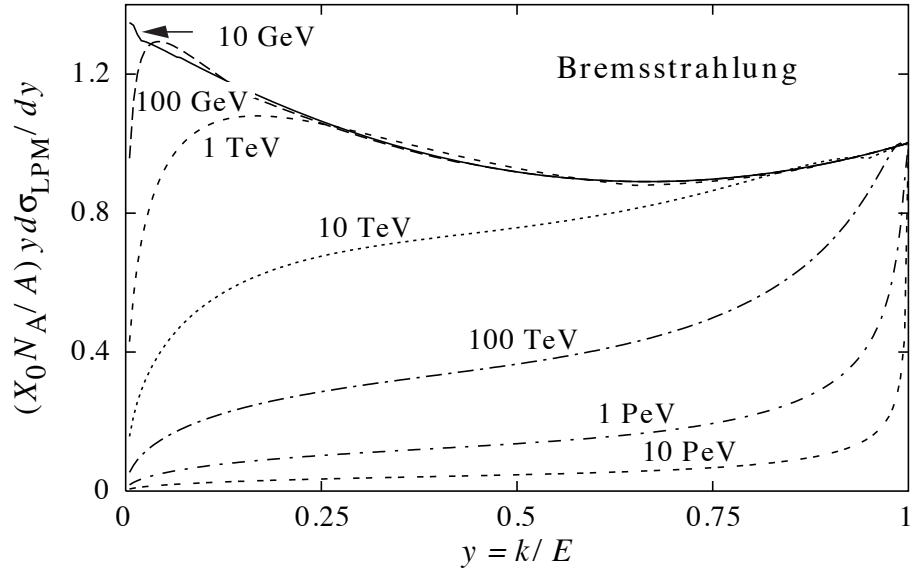


Figure 27.11: The normalized bremsstrahlung cross section $k d\sigma_{LPM}/dk$ in lead versus the fractional photon energy $y = k/E$. The vertical axis has units of photons per radiation length.

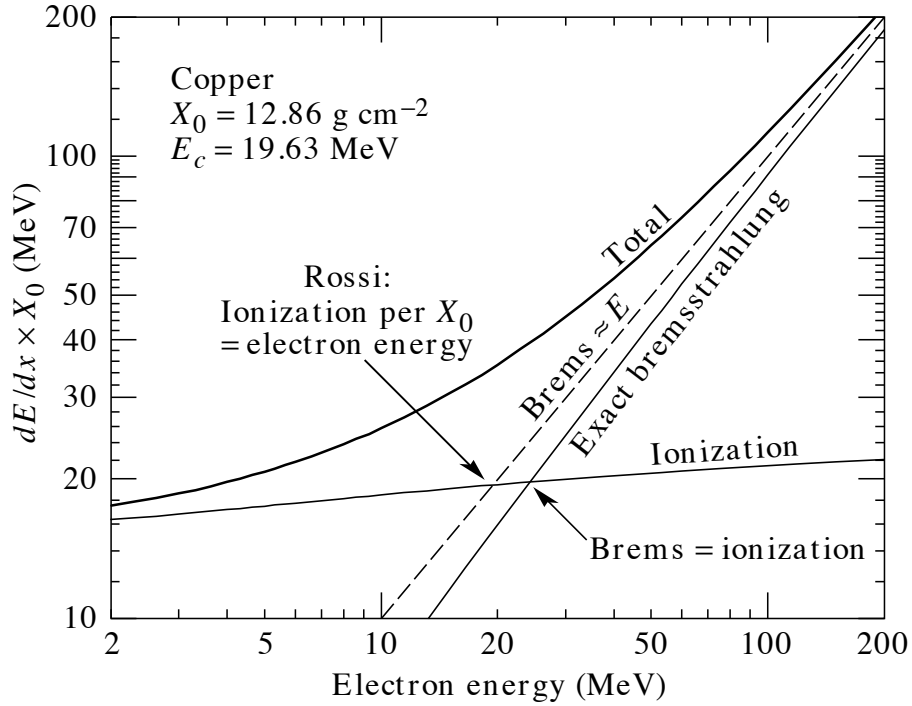


Figure 27.12: Two definitions of the critical energy E_c .

incomplete, and near $y = 0$, where the infrared divergence is removed by the interference of bremsstrahlung amplitudes from nearby scattering centers

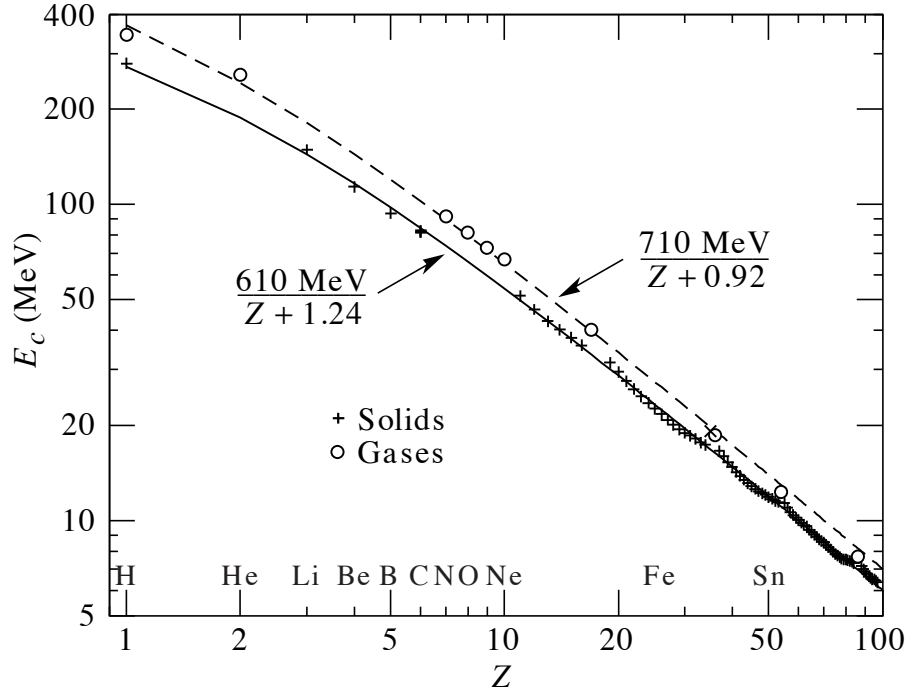


Figure 27.13: Electron critical energy for the chemical elements, using Rossi’s definition [2]. The fits shown are for solids and liquids (solid line) and gases (dashed line). The rms deviation is 2.2% for the solids and 4.0% for the gases. (Computed with code supplied by A. Fassó.)

(the LPM effect) [41,42] and dielectric suppression [43,44]. These and other suppression effects in bulk media are discussed in Sec. 27.4.5.

With decreasing energy ($E \lesssim 10$ GeV) the high- y cross section drops and the curves become rounded as $y \rightarrow 1$. Curves of this familiar shape can be seen in Rossi [2] (Figs. 2.11.2,3); see also the review by Koch & Motz [45].

Except at these extremes, and still in the complete-screening approximation, the number of photons with energies between k_{\min} and k_{\max} emitted by an electron travelling a distance $d \ll X_0$ is

$$N_\gamma = \frac{d}{X_0} \left[\frac{4}{3} \ln \left(\frac{k_{\max}}{k_{\min}} \right) - \frac{4(k_{\max} - k_{\min})}{3E} + \frac{k_{\max}^2 - k_{\min}^2}{2E^2} \right]. \quad (27.28)$$

We obtain

$$E_c = \frac{610 \text{ MeV}}{Z + 1.24} \quad (\text{solids and liquids}), \quad = \frac{710 \text{ MeV}}{Z + 0.92} \quad (\text{gases}).$$

Data from [49]; parameters for $\sigma_{\text{g.d.r.}}$ from [50]. Curves for these and other elements, compounds, and mixtures may be obtained from <http://physics.nist.gov/PhysRefData>. The photon total cross section is approximately flat for at least two decades beyond the energy range shown. Original figures courtesy J.H. Hubbell (NIST).

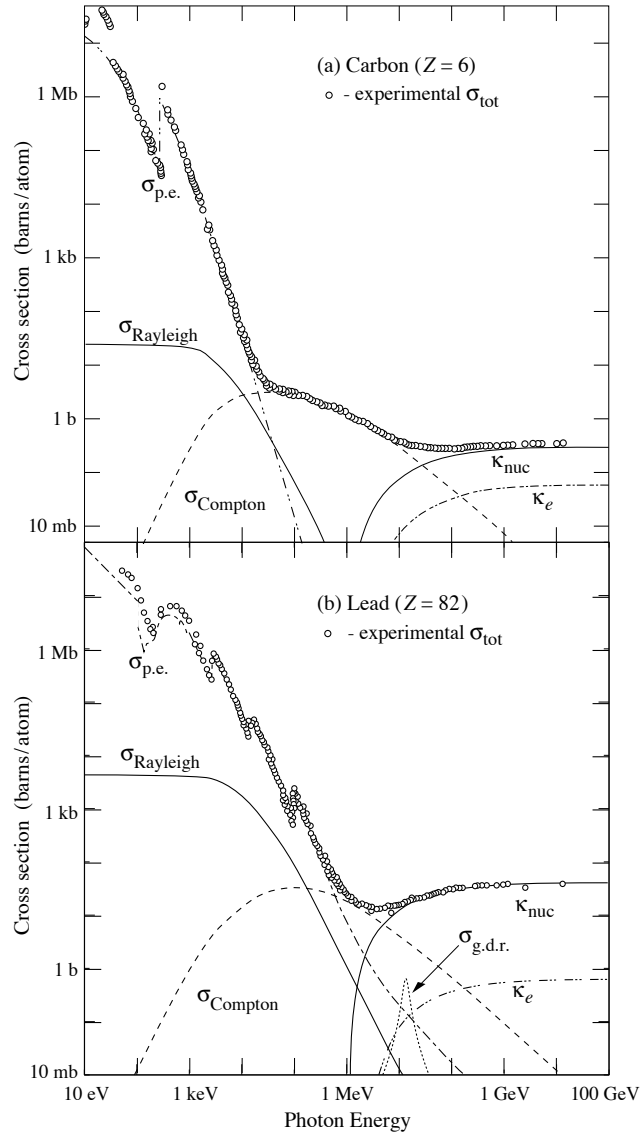


Figure 27.14: Photon total cross sections as a function of energy in carbon and lead, showing the contributions of different processes:

$\sigma_{\text{p.e.}}$ = Atomic photoelectric effect (electron ejection, photon absorption)

σ_{Rayleigh} = Rayleigh (coherent) scattering—atom neither ionized nor excited

σ_{Compton} = Incoherent scattering (Compton scattering off an electron)

κ_{nuc} = Pair production, nuclear field

κ_e = Pair production, electron field

$\sigma_{\text{g.d.r.}}$ = Photonuclear interactions, most notably the Giant Dipole Resonance [48]. In these interactions, the target nucleus is broken up.

27.4.3. Critical energy : An electron loses energy by bremsstrahlung at a

rate nearly proportional to its energy, while the ionization loss rate varies only logarithmically with the electron energy. The *critical energy* E_c is sometimes defined as the energy at which the two loss rates are equal [46]. Berger and Seltzer [46] also give the approximation $E_c = (800 \text{ MeV})/(Z + 1.2)$. This formula has been widely quoted, and has been given in older editions of this *Review* [47]. Among alternate definitions is that of Rossi [2], who defines the critical energy as the energy at which the ionization loss per radiation length is equal to the electron energy. Equivalently, it is the same as the first definition with the approximation $|dE/dx|_{\text{brems}} \approx E/X_0$. This form has been found to describe transverse electromagnetic shower development more accurately (see below). These definitions are illustrated in the case of copper in Fig. 27.12.

The accuracy of approximate forms for E_c has been limited by the failure to distinguish between gases and solid or liquids, where there is a substantial difference in ionization at the relevant energy because of the density effect. We distinguish these two cases in Fig. 27.13. Fits were also made with functions of the form $a/(Z + b)^\alpha$, but α was found to be essentially unity. Since E_c also depends on A , I , and other factors, such forms are at best approximate.

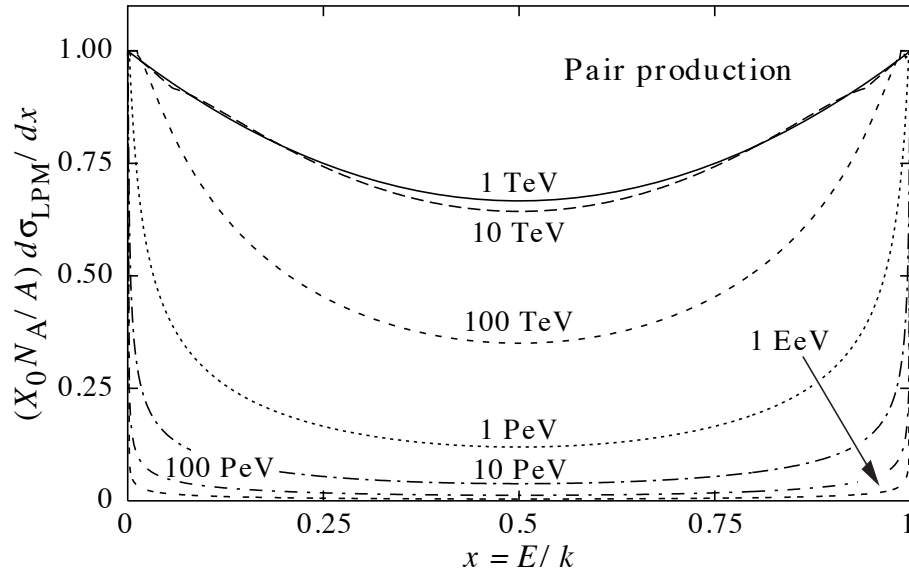


Figure 27.15: The normalized pair production cross section $d\sigma_{LPM}/dy$, versus fractional electron energy $x = E/k$.

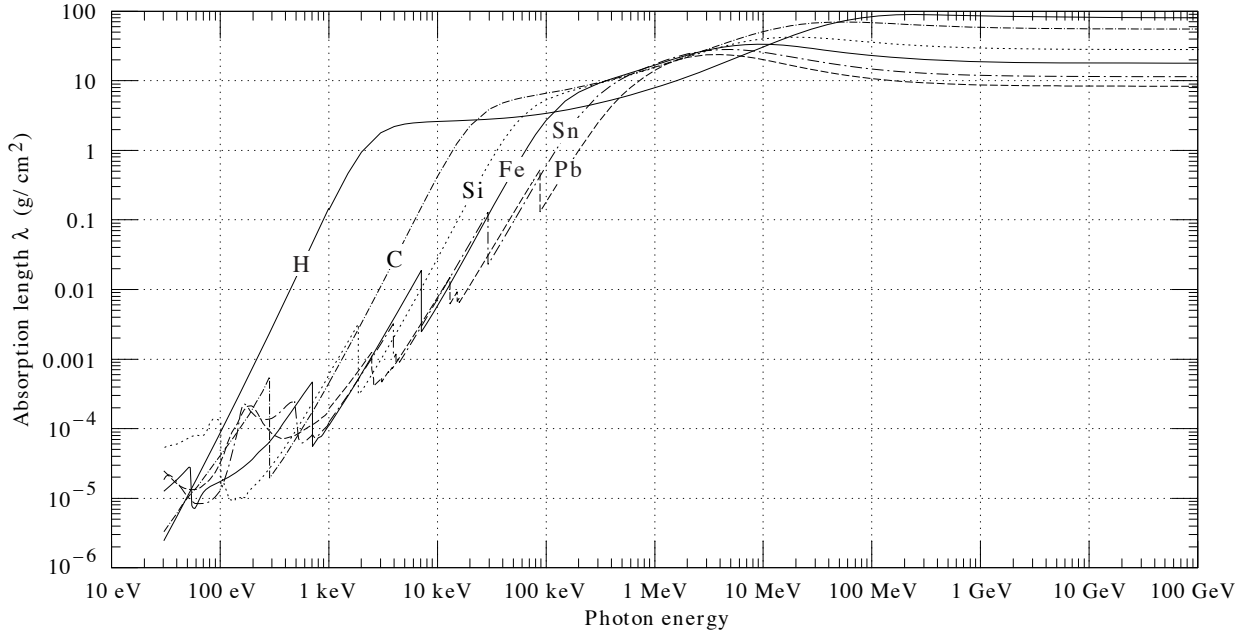


Figure 27.16: The photon mass attenuation length (or mean free path) $\lambda = 1/(\mu/\rho)$ for various elemental absorbers as a function of photon energy. The mass attenuation coefficient is μ/ρ , where ρ is the density. The intensity I remaining after traversal of thickness t (in mass/unit area) is given by $I = I_0 \exp(-t/\lambda)$. The accuracy is a few percent. For a chemical compound or mixture, $1/\lambda_{\text{eff}} \approx \sum_{\text{elements}} w_Z/\lambda_Z$, where w_Z is the proportion by weight of the element with atomic number Z . The processes responsible for attenuation are given in Fig. 27.10. Since coherent processes are included, not all these processes result in energy deposition. The data for $30 \text{ eV} < E < 1 \text{ keV}$ are obtained from http://www-cxro.lbl.gov/optical_constants (courtesy of Eric M. Gullikson, LBNL). The data for $1 \text{ keV} < E < 100 \text{ GeV}$ are from <http://physics.nist.gov/PhysRefData>, through the courtesy of John H. Hubbell (NIST).

27.4.4. Energy loss by photons : Contributions to the photon cross section in a light element (carbon) and a heavy element (lead) are shown in Fig. 27.14. At low energies it is seen that the photoelectric effect dominates, although Compton scattering, Rayleigh scattering, and photonuclear absorption also contribute. The photoelectric cross section is characterized by discontinuities (absorption edges) as thresholds for photoionization of various atomic levels are reached. Photon attenuation lengths for a variety of elements are shown in Fig. 27.16, and data for $30 \text{ eV} < k < 100 \text{ GeV}$ for all elements is available from the web pages given in the caption. Here k is the photon energy.

The increasing domination of pair production as the energy increases is shown

in Fig. 27.17. Using approximations similar to those used to obtain Eq. (27.27), Tsai's formula for the differential cross section [38] reduces to

$$\frac{d\sigma}{dx} = \frac{A}{X_0 N_A} \left[1 - \frac{4}{3}x(1-x) \right] \quad (27.29)$$

in the complete-screening limit valid at high energies. Here $x = E/k$ is the fractional energy transfer to the pair-produced electron (or positron), and k is the incident photon energy. The cross section is very closely related to that for bremsstrahlung, since the Feynman diagrams are variants of one another. The

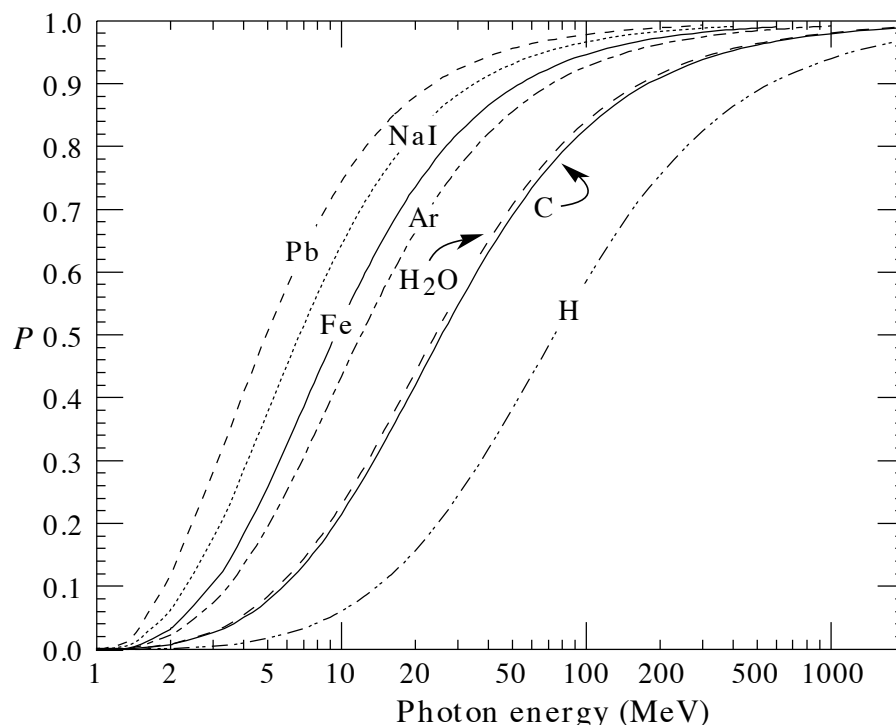


Figure 27.17: Probability P that a photon interaction will result in conversion to an e^+e^- pair. Except for a few-percent contribution from photonuclear absorption around 10 or 20 MeV, essentially all other interactions in this energy range result in Compton scattering off an atomic electron. For a photon attenuation length λ (Fig. 27.16), the probability that a given photon will produce an electron pair (without first Compton scattering) in thickness t of absorber is $P[1 - \exp(-t/\lambda)]$.

cross section is of necessity symmetric between x and $1 - x$, as can be seen by the solid curve in Fig. 27.15. See the review by Motz, Olsen, & Koch for a more detailed treatment [51].

Eq. (27.29) may be integrated to find the high-energy limit for the total e^+e^-

pair-production cross section:

$$\sigma = \frac{7}{9}(A/X_0 N_A) . \quad (27.30)$$

Equation Eq. (27.30) is accurate to within a few percent down to energies as low as 1 GeV, particularly for high- Z materials.

27.4.5. *Bremsstrahlung and pair production at very high energies* : At ultrahigh energies, Eqns. 27.26–27.30 will fail because of quantum mechanical interference between amplitudes from different scattering centers. Since the longitudinal momentum transfer to a given center is small ($\propto k/E(E-k)$, in the case of bremsstrahlung), the interaction is spread over a comparatively long distance called the formation length ($\propto E(E-k)/k$) via the uncertainty principle. In alternate language, the formation length is the distance over which the highly relativistic electron and the photon “split apart.” The interference is usually destructive. Calculations of the “Landau-Pomeranchuk-Migdal” (LPM) effect may be made semi-classically based on the average multiple scattering, or more rigorously using a quantum transport approach [41,42].

In amorphous media, bremsstrahlung is suppressed if the photon energy k is less than $E^2/(E + E_{LPM})$ [42], where*

$$E_{LPM} = \frac{(m_e c^2)^2 \alpha X_0}{4\pi \hbar c \rho} = (7.7 \text{ TeV/cm}) \times \frac{X_0}{\rho} . \quad (27.31)$$

Since physical distances are involved, X_0/ρ , in cm, appears. The energy-weighted bremsstrahlung spectrum for lead, $k d\sigma_{LPM}/dk$, is shown in Fig. 27.11. With appropriate scaling by X_0/ρ , other materials behave similarly.

For photons, pair production is reduced for $E(k-E) > k E_{LPM}$. The pair-production cross sections for different photon energies are shown in Fig. 27.15.

If $k \ll E$, several additional mechanisms can also produce suppression. When the formation length is long, even weak factors can perturb the interaction. For example, the emitted photon can coherently forward scatter off of the electrons in the media. Because of this, for $k < \omega_p E/m_e \sim 10^{-4}$, bremsstrahlung is suppressed by a factor $(k m_e / \omega_p E)^2$ [44]. Magnetic fields can also suppress bremsstrahlung.

In crystalline media, the situation is more complicated, with coherent enhancement or suppression possible. The cross section depends on the electron and photon energies and the angles between the particle direction and the crystalline axes [53].

* This definition differs from that of Ref. 52 by a factor of two. E_{LPM} scales as the 4th power of the mass of the incident particle, so that $E_{LPM} = (1.4 \times 10^{10} \text{ TeV/cm}) \times X_0/\rho$ for a muon.

27.4.6. *Photonuclear and electronuclear interactions at still higher energies*

: At very high photon and electron energies, where the bremsstrahlung and pair production cross-sections are heavily suppressed by the LPM effect, photonuclear and electronuclear interactions predominate over electromagnetic interactions. At photon energies above about 10^{20} eV, for example, photons usually interact hadronically. The exact cross-over energy depends on the model used for the photonuclear interactions. At still higher energies ($\gtrsim 10^{23}$ eV), photonuclear interactions can become coherent, with the photon interaction spread over multiple nuclei. Essentially, the photon coherently converts to a ρ^0 , in a process that is somewhat similar to kaon regeneration [54].

27.5. Electromagnetic cascades

When a high-energy electron or photon is incident on a thick absorber, it initiates an electromagnetic cascade as pair production and bremsstrahlung generate more electrons and photons with lower energy. The longitudinal development is governed by the high-energy part of the cascade, and therefore scales as the radiation length in the material. Electron energies eventually fall below the critical energy, and then dissipate their energy by ionization and excitation rather than by the generation of more shower particles. In describing shower behavior, it is therefore convenient to introduce the scale variables

$$t = x/X_0, \quad y = E/E_c, \quad (27.32)$$

so that distance is measured in units of radiation length and energy in units of critical energy.

Longitudinal profiles from an EGS4 [55] simulation of a 30 GeV electron-induced cascade in iron are shown in Fig. 27.18. The number of particles crossing a plane (very close to Rossi's Π function [2]) is sensitive to the cutoff energy, here chosen as a total energy of 1.5 MeV for both electrons and photons. The electron number falls off more quickly than energy deposition. This is because, with increasing depth, a larger fraction of the cascade energy is carried by photons. Exactly what a calorimeter measures depends on the device, but it is not likely to be exactly any of the profiles shown. In gas counters it may be very close to the electron number, but in glass Cherenkov detectors and other devices with "thick" sensitive regions it is closer to the energy deposition (total track length). In such detectors the signal is proportional to the "detectable" track length T_d , which is in general less than the total track length T . Practical devices are sensitive to electrons with energy above some detection threshold E_d , and $T_d = T F(E_d/E_c)$. An analytic form for $F(E_d/E_c)$ obtained by Rossi [2] is given by Fabjan [56]; see also Amaldi [57].

The mean longitudinal profile of the energy deposition in an electromagnetic

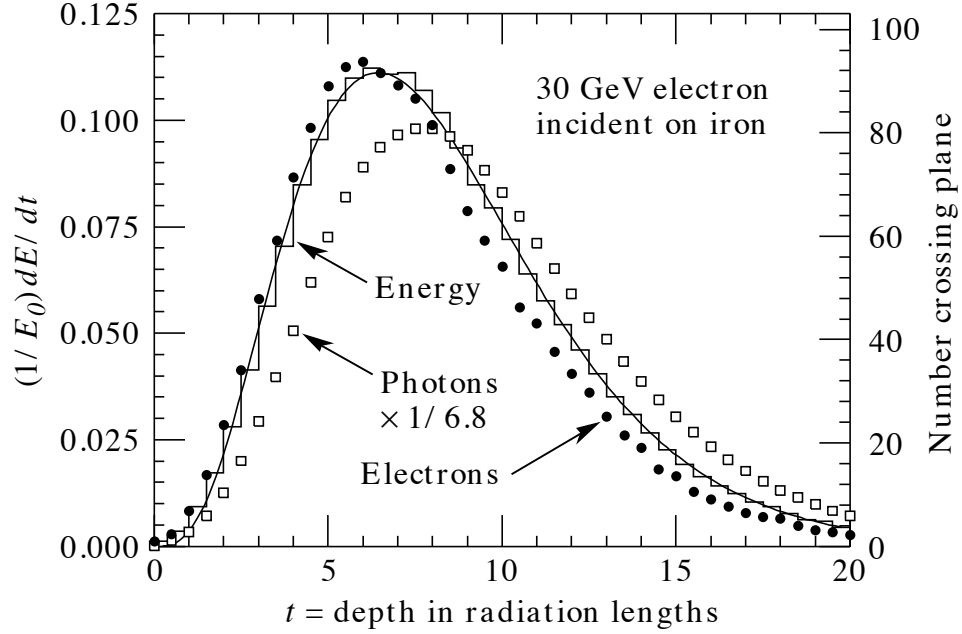


Figure 27.18: An EGS4 simulation of a 30 GeV electron-induced cascade in iron. The histogram shows fractional energy deposition per radiation length, and the curve is a gamma-function fit to the distribution. Circles indicate the number of electrons with total energy greater than 1.5 MeV crossing planes at $X_0/2$ intervals (scale on right) and the squares the number of photons with $E \geq 1.5$ MeV crossing the planes (scaled down to have same area as the electron distribution).

cascade is reasonably well described by a gamma distribution [58]:

$$\frac{dE}{dt} = E_0 b \frac{(bt)^{a-1} e^{-bt}}{\Gamma(a)} \quad (27.33)$$

The maximum t_{\max} occurs at $(a-1)/b$. We have made fits to shower profiles in elements ranging from carbon to uranium, at energies from 1 GeV to 100 GeV. The energy deposition profiles are well described by Eq. (27.33) with

$$t_{\max} = (a-1)/b = 1.0 \times (\ln y + C_j), \quad j = e, \gamma, \quad (27.34)$$

where $C_e = -0.5$ for electron-induced cascades and $C_\gamma = +0.5$ for photon-induced cascades. To use Eq. (27.33), one finds $(a-1)/b$ from Eq. (27.34) and Eq. (27.32), then finds a either by assuming $b \approx 0.5$ or by finding a more accurate value from Fig. 27.19. The results are very similar for the electron number profiles, but there is some dependence on the atomic number of the medium. A similar form for the electron number maximum was obtained by Rossi in the context of his “Approximation B,” [2] (see Fabjan’s review in Ref. 56), but with $C_e = -1.0$ and $C_\gamma = -0.5$; we regard this as superseded by the EGS4 result.

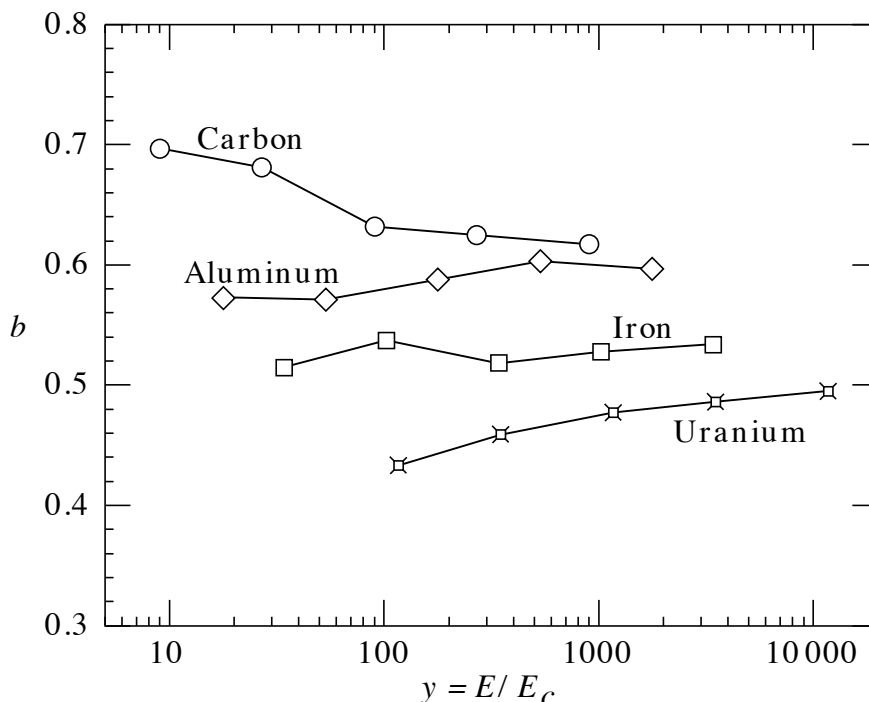


Figure 27.19: Fitted values of the scale factor b for energy deposition profiles obtained with EGS4 for a variety of elements for incident electrons with $1 \leq E_0 \leq 100$ GeV. Values obtained for incident photons are essentially the same.

The “shower length” $X_s = X_0/b$ is less conveniently parameterized, since b depends upon both Z and incident energy, as shown in Fig. 27.19. As a corollary of this Z dependence, the number of electrons crossing a plane near shower maximum is underestimated using Rossi’s approximation for carbon and seriously overestimated for uranium. Essentially the same b values are obtained for incident electrons and photons. For many purposes it is sufficient to take $b \approx 0.5$.

The gamma function distribution is very flat near the origin, while the EGS4 cascade (or a real cascade) increases more rapidly. As a result Eq. (27.33) fails badly for about the first two radiation lengths; it was necessary to exclude this region in making fits.

Because fluctuations are important, Eq. (27.33) should be used only in applications where average behavior is adequate. Grindhammer *et al.* have developed fast simulation algorithms in which the variance and correlation of a and b are obtained by fitting Eq. (27.33) to individually simulated cascades, then generating profiles for cascades using a and b chosen from the correlated distributions [59].

The transverse development of electromagnetic showers in different materials

30 27. Passage of particles through matter

scales fairly accurately with the *Molière radius* R_M , given by [60,61]

$$R_M = X_0 E_s / E_c , \quad (27.35)$$

where $E_s \approx 21$ MeV (Table 27.1), and the Rossi definition of E_c is used.

In a material containing a weight fraction w_j of the element with critical energy E_{cj} and radiation length X_j , the Molière radius is given by

$$\frac{1}{R_M} = \frac{1}{E_s} \sum \frac{w_j E_{cj}}{X_j} . \quad (27.36)$$

Measurements of the lateral distribution in electromagnetic cascades are shown in Refs. 60 and 61. On the average, only 10% of the energy lies outside the cylinder with radius R_M . About 99% is contained inside of $3.5R_M$, but at this radius and beyond composition effects become important and the scaling with R_M fails. The distributions are characterized by a narrow core, and broaden as the shower develops. They are often represented as the sum of two Gaussians, and Grindhammer [59] describes them with the function

$$f(r) = \frac{2r R^2}{(r^2 + R^2)^2} , \quad (27.37)$$

where R is a phenomenological function of x/X_0 and $\ln E$.

At high enough energies, the LPM effect (Sec. 27.4.5) reduces the cross sections for bremsstrahlung and pair production, and hence can cause significant elongation of electromagnetic cascades [42].

27.6. Muon energy loss at high energy

At sufficiently high energies, radiative processes become more important than ionization for all charged particles. For muons and pions in materials such as iron, this “critical energy” occurs at several hundred GeV. (There is no simple scaling with particle mass, but for protons the “critical energy” is much, much higher.) Radiative effects dominate the energy loss of energetic muons found in cosmic rays or produced at the newest accelerators. These processes are characterized by small cross sections, hard spectra, large energy fluctuations, and the associated generation of electromagnetic and (in the case of photonuclear interactions) hadronic showers [62–70]. As a consequence, at these energies the treatment of energy loss as a uniform and continuous process is for many purposes inadequate.

It is convenient to write the average rate of muon energy loss as [71]

$$-dE/dx = a(E) + b(E) E . \quad (27.38)$$

Here $a(E)$ is the ionization energy loss given by Eq. (27.3), and $b(E)$ is the sum of e^+e^- pair production, bremsstrahlung, and photonuclear contributions. To the approximation that these slowly-varying functions are constant, the mean range x_0 of a muon with initial energy E_0 is given by

$$x_0 \approx (1/b) \ln(1 + E_0/E_{\mu c}) , \quad (27.39)$$

where $E_{\mu c} = a/b$. Figure 27.20 shows contributions to $b(E)$ for iron. Since $a(E) \approx 0.002 \text{ GeV g}^{-1} \text{ cm}^2$, $b(E)E$ dominates the energy loss above several hundred GeV, where $b(E)$ is nearly constant. The rates of energy loss for muons in hydrogen, uranium, and iron are shown in Fig. 27.21 [5].

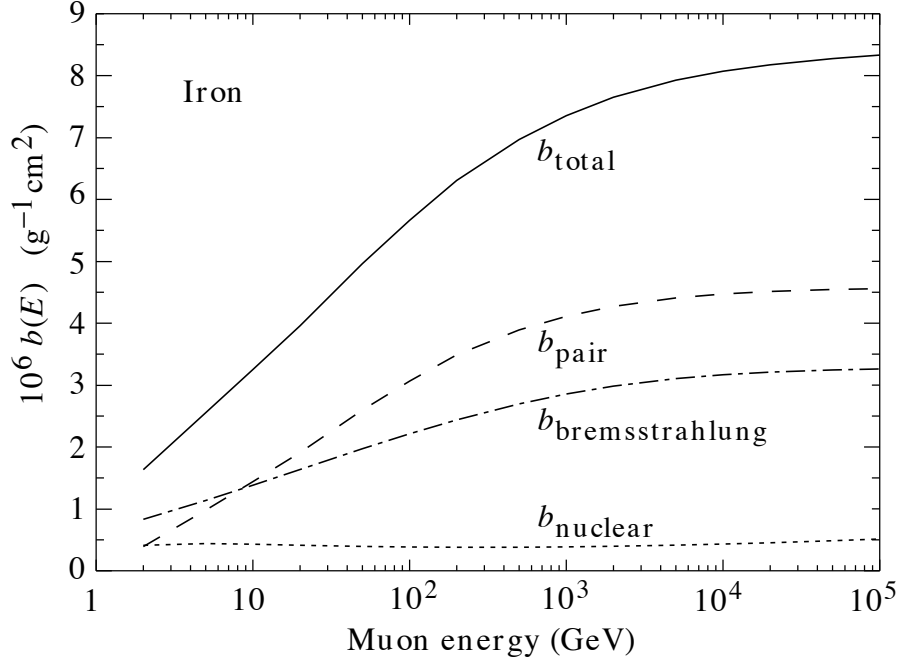


Figure 27.20: Contributions to the fractional energy loss by muons in iron due to e^+e^- pair production, bremsstrahlung, and photonuclear interactions, as obtained from Groom *et al.* [5] except for post-Born corrections to the cross section for direct pair production from atomic electrons.

The “muon critical energy” $E_{\mu c}$ can be defined more exactly as the energy at which radiative and ionization losses are equal, and can be found by solving $E_{\mu c} = a(E_{\mu c})/b(E_{\mu c})$. This definition corresponds to the solid-line intersection in Fig. 27.12, and is different from the Rossi definition we used for electrons. It serves the same function: below $E_{\mu c}$ ionization losses dominate, and above $E_{\mu c}$ radiative effects dominate. The dependence of $E_{\mu c}$ on atomic number Z is shown in Fig. 27.22.

The radiative cross sections are expressed as functions of the fractional energy loss ν . The bremsstrahlung cross section goes roughly as $1/\nu$ over most of the range, while for the pair production case the distribution goes as ν^{-3} to ν^{-2} [72]. “Hard” losses are therefore more probable in bremsstrahlung, and in fact energy losses due to pair production may very nearly be treated as continuous. The simulated [70] momentum distribution of an incident 1 TeV/ c muon beam after it crosses 3 m of iron is shown in Fig. 27.23. The most probable loss is 8 GeV, or $3.4 \text{ MeV g}^{-1} \text{ cm}^2$. The full width at half maximum is 9 GeV/ c , or 0.9%.

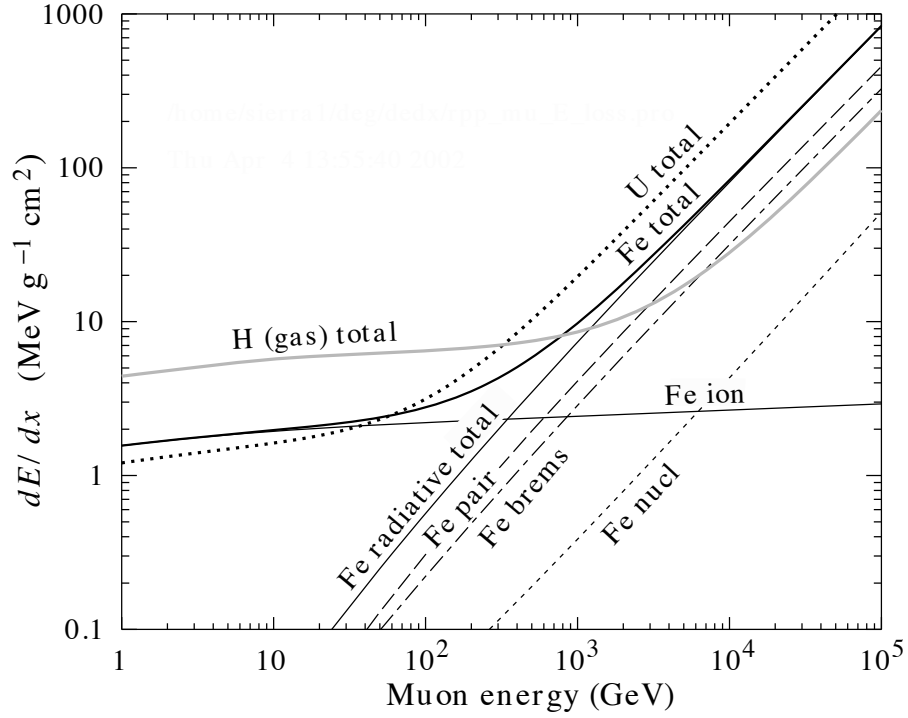


Figure 27.21: The average energy loss of a muon in hydrogen, iron, and uranium as a function of muon energy. Contributions to dE/dx in iron from ionization and the processes shown in Fig. 27.20 are also shown.

The radiative tail is almost entirely due to bremsstrahlung, although most of the events in which more than 10% of the incident energy lost experienced relatively hard photonuclear interactions. The latter can exceed detector resolution [73], necessitating the reconstruction of lost energy. Tables [5] list the stopping power as $9.82 \text{ MeV g}^{-1}\text{cm}^2$ for a 1 TeV muon, so that the mean loss should be 23 GeV ($\approx 23 \text{ GeV}/c$), for a final momentum of 977 GeV/ c , far below the peak. This agrees with the indicated mean calculated from the simulation. Electromagnetic and hadronic cascades in detector materials can obscure muon tracks in detector planes and reduce tracking efficiency [74].

27.7. Cherenkov and transition radiation [75,76,32]

A charged particle radiates if its velocity is greater than the local phase velocity of light (Cherenkov radiation) or if it crosses suddenly from one medium to another with different optical properties (transition radiation). Neither process is important for energy loss, but both are used in high-energy physics detectors.

Cherenkov Radiation. The angle θ_c of Cherenkov radiation, relative to the particle's direction, for a particle with velocity βc in a medium with index of refraction n is

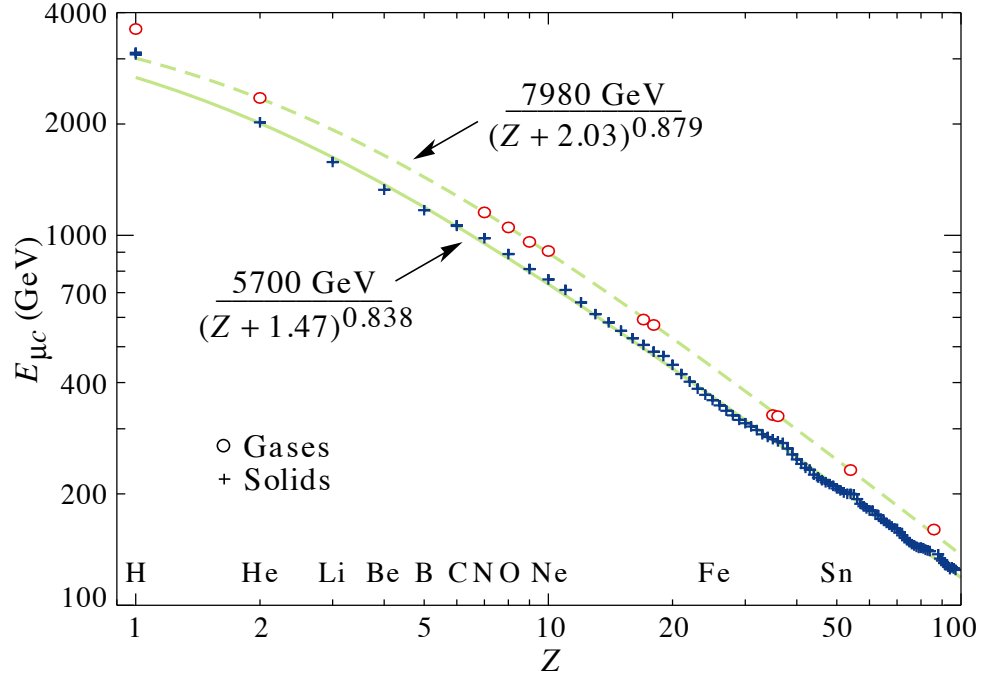


Figure 27.22: Muon critical energy for the chemical elements, defined as the energy at which radiative and ionization energy loss rates are equal [5]. The equality comes at a higher energy for gases than for solids or liquids with the same atomic number because of a smaller density effect reduction of the ionization losses. The fits shown in the figure exclude hydrogen. Alkali metals fall 3–4% above the fitted function, while most other solids are within 2% of the function. Among the gases the worst fit is for radon (2.7% high).

$$\begin{aligned} \cos \theta_c &= (1/n\beta) \\ \text{or } \tan \theta_c &= \sqrt{\beta^2 n^2 - 1} \\ &\approx \sqrt{2(1 - 1/n\beta)} \quad \text{for small } \theta_c, \text{ e.g. in gases.} \end{aligned} \quad (27.40)$$

The threshold velocity β_t is $1/n$, and $\gamma_t = 1/(1 - \beta_t^2)^{1/2}$. Therefore, $\beta_t \gamma_t = 1/(2\delta + \delta^2)^{1/2}$, where $\delta = n - 1$. Values of δ for various commonly used gases are given as a function of pressure and wavelength in Ref. 77. For values at atmospheric pressure, see Table 6.1. Data for other commonly used materials are given in Ref. 78.

Practical Cherenkov radiator materials are dispersive. Let ω be the photon's frequency, and let $k = 2\pi/\lambda$ be its wavenumber. The photons propagate at the group velocity $v_g = d\omega/dk = c/[n(\omega) + \omega(dn/d\omega)]$. In a non-dispersive medium, this simplifies to $v_g = c/n$.

In his classical paper, Tamm [79] showed that for dispersive media the radiation is concentrated in a thin conical shell whose vertex is at the moving charge, and

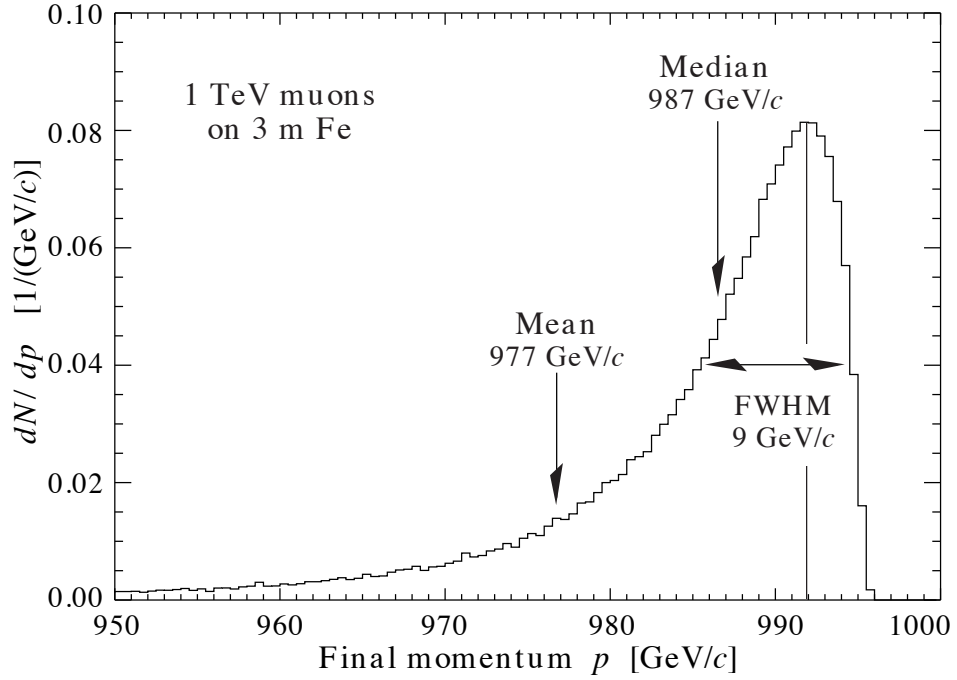


Figure 27.23: The momentum distribution of 1 TeV/ c muons after traversing 3 m of iron as calculated with the MARS15 Monte Carlo code [70] by S.I. Striganov [5].

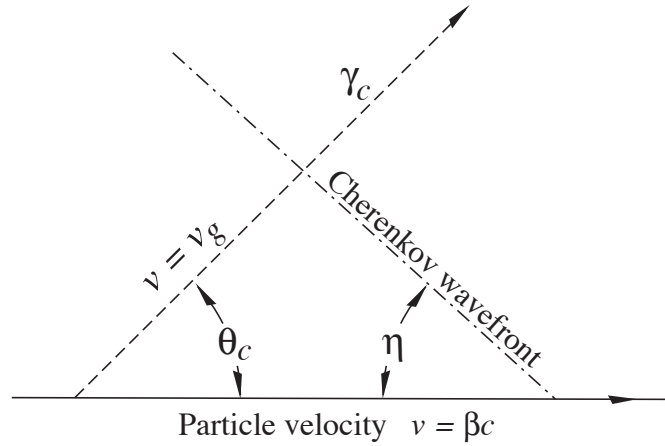


Figure 27.24: Cherenkov light emission and wavefront angles. In a dispersive medium, $\theta_c + \eta \neq 90^\circ$.

whose opening half-angle η is given by

$$\cot \eta = \left[\frac{d}{d\omega} (\omega \tan \theta_c) \right]_{\omega_0}$$

$$= \left[\tan \theta_c + \beta^2 \omega n(\omega) \frac{dn}{d\omega} \cot \theta_c \right]_{\omega_0}, \quad (27.41)$$

where ω_0 is the central value of the small frequency range under consideration. (See Fig. 27.24.) This cone has a opening half-angle η , and, unless the medium is non-dispersive ($dn/d\omega = 0$), $\theta_c + \eta \neq 90^\circ$. The Cherenkov wavefront ‘sideslips’ along with the particle [80]. This effect may have timing implications for ring imaging Cherenkov counters [81], but it is probably unimportant for most applications.

The number of photons produced per unit path length of a particle with charge ze and per unit energy interval of the photons is

$$\begin{aligned} \frac{d^2 N}{dE dx} &= \frac{\alpha z^2}{\hbar c} \sin^2 \theta_c = \frac{\alpha^2 z^2}{r_e m_e c^2} \left(1 - \frac{1}{\beta^2 n^2(E)} \right) \\ &\approx 370 \sin^2 \theta_c(E) \text{ eV}^{-1} \text{ cm}^{-1} \quad (z = 1), \end{aligned} \quad (27.42)$$

or, equivalently,

$$\frac{d^2 N}{dx d\lambda} = \frac{2\pi \alpha z^2}{\lambda^2} \left(1 - \frac{1}{\beta^2 n^2(\lambda)} \right). \quad (27.43)$$

The index of refraction n is a function of photon energy $E = \hbar\omega$, as is the sensitivity of the transducer used to detect the light. For practical use, Eq. (27.42) must be multiplied by the the transducer response function and integrated over the region for which $\beta n(\omega) > 1$. Further details are given in the discussion of Cherenkov detectors in the Particle Detectors section (Sec. 28 of this *Review*).

When two particles are close together (within $\lesssim 1$ wavelength), the electromagnetic fields from the particles may add coherently, affecting the Cherenkov radiation. The radiation from an e^+e^- pair at close separation is suppressed compared to two independent leptons [82].

Coherent radio Cherenkov radiation from electromagnetic showers (containing a net excess of e^- over e^+) is significant [83], and has been used to study cosmic ray air showers [84] and to search for ν_e induced showers.

Transition radiation. The energy radiated when a particle with charge ze crosses the boundary between vacuum and a medium with plasma frequency ω_p is

$$I = \alpha z^2 \gamma \hbar \omega_p / 3, \quad (27.44)$$

where

$$\hbar \omega_p = \sqrt{4\pi N_e r_e^3} m_e c^2 / \alpha = \sqrt{\rho \text{ (in g/cm}^3\text{)} \langle Z/A \rangle} \times 28.81 \text{ eV}. \quad (27.45)$$

For styrene and similar materials, $\hbar \omega_p \approx 20$ eV; for air it is 0.7 eV.

The number spectrum $dN_\gamma/d(\hbar\omega)$ diverges logarithmically at low energies and decreases rapidly for $\hbar\omega/\gamma\hbar\omega_p > 1$. About half the energy is emitted in the range $0.1 \leq \hbar\omega/\gamma\hbar\omega_p \leq 1$. Inevitable absorption in a practical detector removes the

36 27. Passage of particles through matter

divergence. For a particle with $\gamma = 10^3$, the radiated photons are in the soft x-ray range 2 to 40 keV. The γ dependence of the emitted energy thus comes from the hardening of the spectrum rather than from an increased quantum yield.

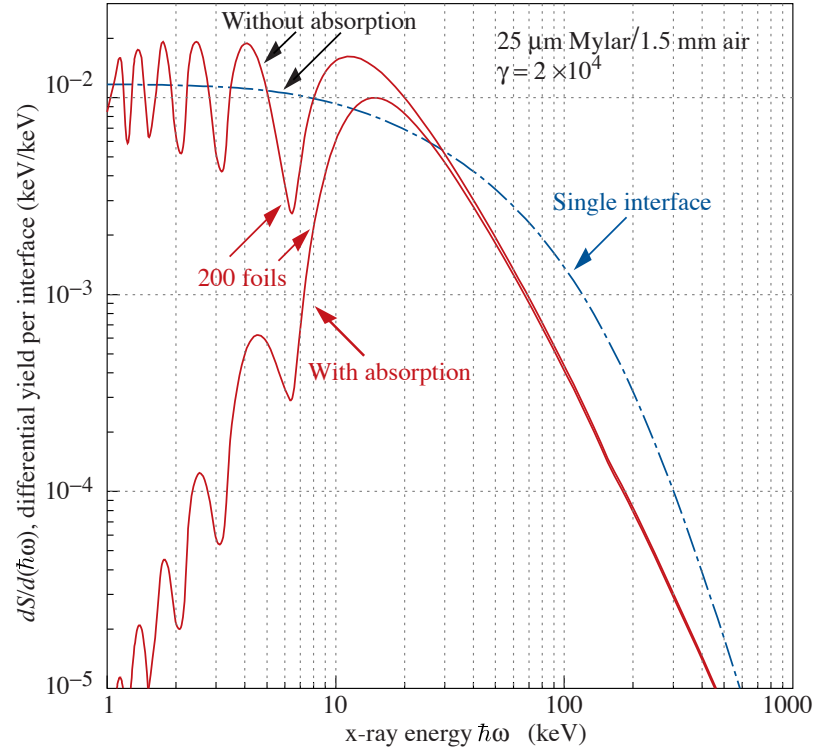


Figure 27.25: X-ray photon energy spectra for a radiator consisting of 200 25 μm thick foils of Mylar with 1.5 mm spacing in air (solid lines) and for a single surface (dashed line). Curves are shown with and without absorption. Adapted from Ref. 85.

The number of photons with energy $\hbar\omega > \hbar\omega_0$ is given by the answer to problem 13.15 in Ref. 32,

$$N_\gamma(\hbar\omega > \hbar\omega_0) = \frac{\alpha z^2}{\pi} \left[\left(\ln \frac{\gamma \hbar\omega_p}{\hbar\omega_0} - 1 \right)^2 + \frac{\pi^2}{12} \right], \quad (27.46)$$

within corrections of order $(\hbar\omega_0/\gamma\hbar\omega_p)^2$. The number of photons above a fixed energy $\hbar\omega_0 \ll \gamma\hbar\omega_p$ thus grows as $(\ln \gamma)^2$, but the number above a fixed fraction of $\gamma\hbar\omega_p$ (as in the example above) is constant. For example, for $\hbar\omega > \gamma\hbar\omega_p/10$, $N_\gamma = 2.519 \alpha z^2/\pi = 0.59\% \times z^2$.

The particle stays “in phase” with the x ray over a distance called the formation length, $d(\omega)$. Most of the radiation is produced in a distance $d(\omega) = (2c/\omega)(1/\gamma^2 + \theta^2 + \omega_p^2/\omega^2)^{-1}$. Here θ is the x-ray emission angle, characteristically $1/\gamma$. For $\theta = 1/\gamma$ the formation length has a maximum at $d(\gamma\omega_p/\sqrt{2}) = \gamma c/\sqrt{2}\omega_p$. In practical situations it is tens of μm .

Since the useful x-ray yield from a single interface is low, in practical detectors it is enhanced by using a stack of N foil radiators—foils L thick, where L is typically several formation lengths—separated by gas-filled gaps. The amplitudes at successive interfaces interfere to cause oscillations about the single-interface spectrum. At increasing frequencies above the position of the last interference maximum ($L/d(w) = \pi/2$), the formation zones, which have opposite phase, overlap more and more and the spectrum saturates, $dI/d\omega$ approaching zero as $L/d(\omega) \rightarrow 0$. This is illustrated in Fig. 27.25 for a realistic detector configuration.

For regular spacing of the layers fairly complicated analytic solutions for the intensity have been obtained [85]. (See also Ref. 86 and references therein.) Although one might expect the intensity of coherent radiation from the stack of foils to be proportional to N^2 , the angular dependence of the formation length conspires to make the intensity $\propto N$.

References:

1. H. Bichsel, Nucl. Instrum. Methods **A562**, 154–197 (2006).
2. B. Rossi, *High Energy Particles*, Prentice-Hall, Inc., Englewood Cliffs, NJ, 1952.
3. H.A. Bethe, *Zur Theorie des Durchgangs schneller Korpuskularstrahlen durch Materie*, H. Bethe, Ann. Phys. **5**, 325 (1930).
4. “Stopping Powers and Ranges for Protons and Alpha Particles,” ICRU Report No. 49 (1993);
Tables and graphs of these data are available at
<http://physics.nist.gov/PhysRefData/>.
5. D.E. Groom, N.V. Mokhov, and S.I. Striganov, “Muon stopping-power and range tables: 10 MeV–100 TeV,” Atomic Data and Nuclear Data Tables **78**, 183–356 (2001). Since submission of this paper it has become likely that post-Born corrections to the direct pair production cross section should be made. Code used to make Figs. 27.20–27.22 included these corrections [D.Yu. Ivanov *et al.*, Phys. Lett. **B442**, 453 (1998)]. The effect is negligible for except at high Z . (It is less than 1% for iron.);
More extensive printable and machine-readable tables are given at
<http://pdg.lbl.gov/AtomicNuclearProperties/>.
6. W.H. Barkas, W. Birnbaum, and F.M. Smith, Phys. Rev. **101**, 778 (1956).
7. U. Fano, Ann. Rev. Nucl. Sci. **13**, 1 (1963).
8. J. D. Jackson, Phys. Rev. **D59**, 017301 (1999).
9. S.M. Seltzer and M.J. Berger, Int. J. of Applied Rad. **33**, 1189 (1982).
10. “Stopping Powers for Electrons and Positrons,” ICRU Report No. 37 (1984).
11. <http://physics.nist.gov/PhysRefData/XrayMassCoef/tab1.html>.
12. H. Bichsel, Phys. Rev. **A46**, 5761 (1992).
13. W.H. Barkas and M.J. Berger, *Tables of Energy Losses and Ranges of Heavy Charged Particles*, NASA-SP-3013 (1964).

38 27. *Passage of particles through matter*

14. M. Agnello *et al.*, Phys. Rev. Lett. **74**, 371 (1995).
15. H.H. Andersen and J.F. Ziegler, *Hydrogen: Stopping Powers and Ranges in All Elements*. Vol. 3 of *The Stopping and Ranges of Ions in Matter* (Pergamon Press 1977).
16. J. Lindhard, Kgl. Danske Videnskab. Selskab, Mat.-Fys. Medd. **28**, No. 8 (1954);
J. Lindhard, M. Scharff, and H.E. Schiøtt, Kgl. Danske Videnskab. Selskab, Mat.-Fys. Medd. **33**, No. 14 (1963).
17. J.F. Ziegler, J.F. Biersac, and U. Littmark, *The Stopping and Range of Ions in Solids*, Pergamon Press 1985.
18. R.M. Sternheimer, Phys. Rev. **88**, 851 (1952).
19. A. Crispin and G.N. Fowler, Rev. Mod. Phys. **42**, 290 (1970).
20. R.M. Sternheimer, S.M. Seltzer, and M.J. Berger, "The Density Effect for the Ionization Loss of Charged Particles in Various Substances," Atomic Data and Nuclear Data Tables **30**, 261 (1984). Minor errors are corrected in Ref. 5. Chemical composition for the tabulated materials is given in Ref. 9.
21. R.M. Sternheimer and R.F. Peierls, Phys. Rev. **B3**, 3681 (1971).
22. For unit-charge projectiles, see E.A. Uehling, Ann. Rev. Nucl. Sci. **4**, 315 (1954). For highly charged projectiles, see J.A. Doggett and L.V. Spencer, Phys. Rev. **103**, 1597 (1956). A Lorentz transformation is needed to convert these center-of-mass data to knock-on energy spectra.
23. N.F. Mott and H.S.W. Massey, *The Theory of Atomic Collisions*, Oxford Press, London, 1965.
24. L.D. Landau, J. Exp. Phys. (USSR) **8**, 201 (1944).
25. P.V. Vavilov, Sov. Phys. JETP **5**, 749 (1957).
26. H. Bichsel, Rev. Mod. Phys. **60**, 663 (1988).
27. R. Talman, Nucl. Instrum. Methods **159**, 189 (1979).
28. S.M. Seltzer and M.J. Berger, Int. J. of Applied Rad. **35**, 665 (1984). This paper corrects and extends the results of Ref. 9.
29. L.V. Spencer "Energy Dissipation by Fast Electrons," Nat'l Bureau of Standards Monograph No. 1 (1959).
30. "Average Energy Required to Produce an Ion Pair," ICRU Report No. 31 (1979).
31. N. Hadley *et al.*, "List of Poisoning Times for Materials," Lawrence Berkeley Lab Report TPC-LBL-79-8 (1981).
32. J.D. Jackson, *Classical Electrodynamics*, 3rd edition, (John Wiley & Sons, New York, 1998).
33. H.A. Bethe, Phys. Rev. **89**, 1256 (1953). A thorough review of multiple scattering is given by W.T. Scott, Rev. Mod. Phys. **35**, 231 (1963). However, the data of Shen *et al.*, (Phys. Rev. **D20**, 1584 (1979)) show that Bethe's simpler method of including atomic electron effects agrees better

- with experiment that does Scott's treatment. For a thorough discussion of simple formulae for single scatters and methods of compounding these into multiple-scattering formulae, see W.T. Scott, *Rev. Mod. Phys.* **35**, 231 (1963). Detailed summaries of formulae for computing single scatters are given in J.W. Motz, H. Olsen, and H.W. Koch, *Rev. Mod. Phys.* **36**, 881 (1964).
34. V.L. Highland, *Nucl. Instrum. Methods* **129**, 497 (1975), and *Nucl. Instrum. Methods* **161**, 171 (1979).
 35. G.R. Lynch and O.I Dahl, *Nucl. Instrum. Methods* **B58**, 6 (1991).
 36. M. Wong *et al.*, *Med. Phys.* **17**, 163 (1990).
 37. E. Segré, *Nuclei and Particles*, New York, Benjamin (1964) p. 65 ff.
 38. Y.S. Tsai, *Rev. Mod. Phys.* **46**, 815 (1974).
 39. H. Davies, H.A. Bethe, and L.C. Maximon, *Phys. Rev.* **93**, 788 (1954).
 40. O.I. Dahl, private communication.
 41. L.D. Landau and I.J. Pomeranchuk, *Dokl. Akad. Nauk. SSSR* **92**, 535 (1953); **92**, 735 (1953). These papers are available in English in L. Landau, *The Collected Papers of L.D. Landau*, Pergamon Press, 1965; A.B. Migdal, *Phys. Rev.* **103**, 1811 (1956).
 42. S. Klein, *Rev. Mod. Phys.* **71**, 1501 (1999).
 43. M. L. Ter-Mikaelian, *SSSR* **94**, 1033 (1954);
M. L. Ter-Mikaelian, *High Energy Electromagnetic Processes in Condensed Media* (John Wiley & Sons, New York, 1972).
 44. P. Anthony *et al.*, *Phys. Rev. Lett.* **76**, 3550 (1996).
 45. H. W. Koch and J. W. Motz, *Rev. Mod. Phys.* **31**, 920 (1959).
 46. M.J. Berger and S.M. Seltzer, "Tables of Energy Losses and Ranges of Electrons and Positrons," National Aeronautics and Space Administration Report NASA-SP-3012 (Washington DC 1964).
 47. K. Hikasa *et al.*, *Review of Particle Properties*, *Phys. Rev.* **D46** (1992) S1.
 48. B. L. Berman and S. C. Fultz, *Rev. Mod. Phys.* **47**, 713 (1975).
 49. J.S. Hubbell, H. Gimm, and I Øverbø, *J. Phys. Chem. Ref. Data* **9**, 1023 (1980).
 50. A. Veyssiere *et al.*, *Nucl. Phys.* **A159**, 561 (1970).
 51. J. W. Motz, H. A. Olsen, and H. W. Koch, *Rev. Mod. Phys.* **41**, 581 (1969).
 52. P. Anthony *et al.*, *Phys. Rev. Lett.* **75**, 1949 (1995).
 53. U.I. Uggerhoj, *Rev. Mod. Phys.* **77**, 1131 (2005).
 54. FIND IT..
 55. W.R. Nelson, H. Hirayama, and D.W.O. Rogers, "The EGS4 Code System," SLAC-265, Stanford Linear Accelerator Center (Dec. 1985).
 56. *Experimental Techniques in High Energy Physics*, ed. by T. Ferbel (Addison-Wesley, Menlo Park CA 1987).
 57. U. Amaldi, *Phys. Scripta* **23**, 409 (1981).

40 27. *Passage of particles through matter*

58. E. Longo and I. Sestili, Nucl. Instrum. Methods **128**, 283 (1975).
59. G. Grindhammer *et al.*, in *Proceedings of the Workshop on Calorimetry for the Supercollider*, Tuscaloosa, AL, March 13–17, 1989, edited by R. Donaldson and M.G.D. Gilchriese (World Scientific, Teaneck, NJ, 1989), p. 151.
60. W.R. Nelson *et al.*, Phys. Rev. **149**, 201 (1966).
61. G. Bathow *et al.*, Nucl. Phys. **B20**, 592 (1970).
62. H.A. Bethe and W. Heitler, *Proc. Roy. Soc.* **A146**, 83 (1934);
H.A. Bethe, *Proc. Cambridge Phil. Soc.* **30**, 542 (1934).
63. A.A. Petrukhin and V.V. Shestakov, Can. J. Phys. **46**, S377 (1968).
64. V.M. Galitskii and S.R. Kel’ner, Sov. Phys. JETP **25**, 948 (1967).
65. S.R. Kel’ner and Yu.D. Kotov, Sov. J. Nucl. Phys. **7**, 237 (1968).
66. R.P. Kokoulin and A.A. Petrukhin, in *Proceedings of the International Conference on Cosmic Rays*, Hobart, Australia, August 16–25, 1971, Vol. **4**, p. 2436.
67. A.I. Nikishov, Sov. J. Nucl. Phys. **27**, 677 (1978).
68. Y.M. Andreev *et al.*, Phys. Atom. Nucl. **57**, 2066 (1994).
69. L.B. Bezrukov and E.V. Bugaev, Sov. J. Nucl. Phys. **33**, 635 (1981).
70. N.V. Mokhov, “The MARS Code System User’s Guide,” Fermilab-FN-628 (1995);
N. V. Mokhov *et al.*, Radiation Protection and Dosimetry, vol. 116, part 2, pp. 99 (2005);
Fermilab-Conf-04/053 (2004);
N. V. Mokhov *et al.*, in *Proc. of Intl. Conf. on Nuclear Data for Science and Tech.*, (Santa Fe, NM, 2004), AIP Conf. Proc. 769, part 2, p. 1618;
Fermilab-Conf-04/269-AD (2004);
<http://www-ap.fnl.gov/MARS/>.
71. P.H. Barrett *et al.*, Rev. Mod. Phys. **24**, 133 (1952).
72. A. Van Ginneken, Nucl. Instrum. Methods **A251**, 21 (1986).
73. U. Becker *et al.*, Nucl. Instrum. Methods **A253**, 15 (1986).
74. J.J. Eastman and S.C. Loken, in *Proceedings of the Workshop on Experiments, Detectors, and Experimental Areas for the Supercollider*, Berkeley, CA, July 7–17, 1987, edited by R. Donaldson and M.G.D. Gilchriese (World Scientific, Singapore, 1988), p. 542.
75. *Methods of Experimental Physics*, L.C.L. Yuan and C.-S. Wu, editors, Academic Press, 1961, Vol. 5A, p. 163.
76. W.W.M. Allison and P.R.S. Wright, “The Physics of Charged Particle Identification: dE/dx , Cherenkov Radiation, and Transition Radiation,” p. 371 in *Experimental Techniques in High Energy Physics*, T. Ferbel, editor, (Addison-Wesley 1987).
77. E.R. Hayes, R.A. Schluter, and A. Tamosaitis, “Index and Dispersion of Some Cherenkov Counter Gases,” ANL-6916 (1964).

- 78. T. Ypsilantis, “Particle Identification at Hadron Colliders”, CERN-EP/89-150 (1989), or ECFA 89-124, **2** 661 (1989).
- 79. I. Tamm, J. Phys. U.S.S.R., **1**, 439 (1939).
- 80. H. Motz and L. I. Schiff, Am. J. Phys. **21**, 258 (1953).
- 81. B. N. Ratcliff, Nucl. Instrum & Meth. **A502**, 211 (2003).
- 82. S. K. Mandal, S. R. Klein, and J. D. Jackson, Phys. Rev. **D72**, 093003 (2005).
- 83. E. Zas, F. Halzen and T. Stanev, Phys. Rev. **D45**, 362 (1991).
- 84. H. Falcke *et al*, Nature **435**, 313 (2005).
- 85. M. L. Cherry, Phys. Rev. **D10**, 3594–3607 (1974);
M. L. Cherry, Phys. Rev. **D17**, 2245–2260 (1978).
- 86. B. Dolgoshein, Nucl. Instrum. Methods **A326**, 434–469 (1993).